Chromatin remodeling protein CHD4 regulates axon guidance of spiral ganglion neurons in the developing cochlea

Jihyun Kim[1,2,*], Edward Martinez[1,2,*], Jingyun Qiu[2], Julie Zhouli Ni[3], Kelvin Y. Kwan[1,2]

[1]Keck Center for Collaborative Neuroscience and Stem Cell Research Center, Rutgers University, Piscataway, NJ 08854, USA

[2]Department of Cell Biology and Neuroscience, Rutgers University, Piscataway, NJ 08854, USA

[3] Department of Molecular Biology and Biochemistry, Rutgers University, Piscataway, NJ 08854, USA

* J.K. and E.M. contributed equally to this work.

Corresponding Author:

Kelvin Y. Kwan

Address: 604 Allison Road, D250 Nelson Labs, Piscataway, NJ 08854

Email: kwan@dls.rutgers.edu

Running Title: CHD4 axon guidance

Key Words: CHD4, spiral ganglion neurons, axon guidance, epigenetics, chromatin remodeling

Word Count:

Number of Figures: 6

Number of Tables: 3

Number of Supplemental Figures: 5

Number of Supplemental Tables: 1

Abstract (191 words)

Spiral ganglion neurons (SGNs) are the primary afferent neurons that convey sound information from the cochlea, but the epigenetic changes that occur during development are unknown. We identified the chromodomain helicase binding protein 4 (CHD4) expression in SGNs. CHD4 is an ATP-dependent chromatin remodeler. We employed the *Neurog1* (*Ngn1*) CreERT^2 *Chd4* conditional knockout animals to investigate *Chd4* function in SGNs. SGNs are classified as type I and II neurons with different innervation patterns. SGNs lacking CHD4 showed abnormal fasciculation of type I neurons along with improper pathfinding of type II fibers. CHD4 binding to chromatin from immortalized multipotent otic progenitor-derived neurons was used to identify candidate target genes in SGNs. Gene ontology analysis of CHD4 target genes revealed cellular processes involved in axon guidance, axonal fasciculation, and the ephrin receptor signaling pathway. Eph/ephrin signaling regulates various biological processes, including axon guidance. We confirmed increased Eph/ephrin transcripts in SGNs from *Chd4* conditional knockout cochleae. The results implicate epigenetic changes in circuit wiring by modulating the expression of a subset of axon guidance molecules. The results also provide insights into neurodevelopmental diseases such as Sifrim-Hitz-Weiss syndrome (SIHIWES) and inform strategies for regenerating SGNs.

Introduction

Spiral ganglion neurons (SGNs) in the cochlea are essential for conveying sound information from the cochlear hair cells to the brainstem (Dabdoub, Fritzsch et al. 2016). Assembly of these specialized neural circuits and the rules that govern the complexity require distinct developmental steps and activity-dependent synaptic refinement (Sitko and Goodrich 2021). SGNs are categorized as type I and type II neurons. Type I neurons are large, myelinated, and comprise ~95% of the SGNs that form a single synapse with inner hair cells of the cochlea. Type II neurons are small, unmyelinated neurons, constituting about 5% of the SGNs. Each type II SGN contacts multiple outer hair cells to form *en passant* synapses (Liberman, Wang et al. 2011, Weisz, Lehar et al. 2012, Moser, Karagulyan et al. 2023). The innervation pattern of type I and type II SGNs occurs through a series of defined stages. During early development, neurosensory precursors marked by the expression of *Neurog1*, a key transcription factor required for SGN development, give rise to spiral ganglion neurons (SGNs). Starting around embryonic day 10 (E10), the *Neurog1*-expressing precursors delaminate from the otic vesicle by E11, forming neuronal precursors. Between E12-14, SGNs extend their peripheral axons towards the cochlear hair cells and central axons towards the brainstem. By E15, initial innervation patterns are established between SGNs, their target hair cells, and the cochlear nucleus in the brainstem. Starting at E16, the neural circuits undergo refinement through activity-dependent mechanisms that involve synapse formation and refinement (Appler and Goodrich 2011, Coate and Kelley 2013). The initial establishment of circuit assembly in spiral ganglion neurons (SGNs) requires cellular processes such as axon guidance and repulsion cues to pattern and assemble the circuits (Sitko and Goodrich 2021). How genes involved in axon guidance are regulated is not well understood.

Epigenetic changes can significantly influence the expression of axon guidance genes during development. Changes such as DNA methylation and histone modifications can control gene expression patterns and the timing of guidance cues. For instance, epigenetic modifications can regulate the

27 expression of genes encoding guidance molecules like netrins, ephrins, slits, semaphorins and
28 neuropilin, which are essential for directing peripheral axon patterns (Gillespie, Marzella et al. 2005,
29 Coate, Raft et al. 2012, Defourny, Poirrier et al. 2013, Coate, Spita et al. 2015, Kim, Ibrahim et al. 2016,
30 Salehi, Ge et al. 2017). By modulating accessibility to cis-regulatory elements that control the
31 transcription of these genes, epigenetic changes can regulate the timing and expression levels of axon
32 guidance genes to control wiring.
33
34 Mutations in genes that code for epigenetic modifiers that cause syndromic hearing loss implicate these
35 molecules in cochlear development. Pathogenic variants in DNA methyltransferases (DNMT1), histone
36 methyltransferases (EHMT1, KMT2D), acetyltransferase (KAT6B), and the chromodomain helicase DNA
37 binding (CHD) protein family are associated with hearing loss (Layman and Zuo 2014). The CHD family
38 of proteins mobilizes and rearranges nucleosomes to alter chromatin accessibility. Pathogenic variants
39 in CHD4 and CHD7 are associated with Sifrim-Hitz-Weiss and CHARGE syndrome, respectively
40 (Micucci, Sperry et al. 2015, Clapier, Iwasa et al. 2017). Sifrim-Hitz-Weiss (SIHIWES) is an autosomal
41 dominant intellectual developmental disorder with variable congenital abnormalities. Patients with
42 SIHIWES show delayed development, intellectual disability, facial dysmorphism, and ear abnormalities,
43 including hearing loss (Sifrim, Hitz et al. 2016, Weiss, Terhal et al. 2016). Hearing loss in patients with
44 SIHIWES is confounded by the potential function of CHD4 in many different inner ear cell types during
45 development. In the mouse, the expression of CHD4 and components of the nucleosome remodeling
46 and deacetylase (NuRD) complex are detected in many types of cells in the cochlear sensory epithelium
47 (Layman, Sauceda et al. 2013). CHD4 has been studied in the context of the NuRD complex (Tong,
48 Hassig et al. 1998, Xue, Wong et al. 1998, Zhang, LeRoy et al. 1998). Paralogs from six protein families
49 form the core NuRD complex (Torchy, Hamiche et al. 2015, Millard, Varma et al. 2016). Multiple paralogs
50 from each protein family can form distinct NuRD complexes (Torrado, Low et al. 2017). The ATP-
51 dependent nucleosome remodeler CHD4 and the histone deacetylases (HDAC1, HDAC2) form the
52 catalytic subunits. Other members include the methyl binding proteins (MBD2, MBD3), and structural

53 subunits (MTA1, MTA2, MTA3, GATAD2A, GATAD2B, RBBP4, RBBP7). The NuRD complex localizes
54 to different cis-regulatory elements to affect gene expression (Morra, Lee et al. 2012, Watson, Mahajan
55 et al. 2012, Marques, Gryder et al. 2020).
56
57 A decrease in transcription caused by the NuRD complex affects a myriad of cellular processes, including
58 maintenance of cell identity, DNA damage repair, cell cycle progression, and cancer (Polo, Kaidi et al.
59 2010, Hung, Kohnken et al. 2012, Pan, Hsieh et al. 2012, Hosokawa, Tanaka et al. 2013, Yang, Yamada
60 et al. 2016, Xia, Huang et al. 2017, Bornelov, Reynolds et al. 2018, Marques, Gryder et al. 2020). CHD4
61 binds to thousands of sites in the mammalian genome in a cell-type-specific manner, and studies show
62 that CHD4 forms distinct protein complexes with NuRD-independent functions (Low, Webb et al. 2016,
63 Hoffmeister, Fuchs et al. 2017, Kaaij, Mohn et al. 2019). To clarify the function of CHD4, we employed a
64 conditional knockout model to understand CHD4's function in developing spiral ganglion neurons (SGNs).
65 SGNs are the primary afferent neurons in the cochlea that convey auditory signals from the sensory hair
66 cells to the cochlear nucleus in the brainstem. Improper function of SGNs could result in sensorineural
67 hearing loss. We examined *Chd4* function in SGNs using a transgenic mouse line harboring the
68 *Neurog1*(*Ngn1*) CreER^{T2} (Koundakjian, Appler et al. 2007), *Chd4* conditional knockout (cKO) alleles
69 (Williams, Naito et al. 2004), and a tdTomato reporter (Madisen, Zwingman et al. 2010).

Materials and Methods

Generation of *Chd4* conditional knockout mice

All procedures were based on institutional animal care, used committee research guidelines, and were done at Rutgers University. *Chd4*$^{tm1Kge/tm1Kge}$ (*Chd4* floxed*)* animals (RRID: MGI:3641408) were obtained from Dr. Katia Georgopoulos (Williams, Naito et al. 2004). Neurog1(Ngn1) CreER^{T2} animals and Ai9 R26R tdTomato reporter animals were purchased from Jackson Laboratory (RRID: IMSR_JAX:008529 and RRID: IMSR_JAX:007909, respectively) (Koundakjian, Appler et al. 2007, Madisen, Zwingman et al. 2010). PCR genotyping was performed using the EconoTaq Plus Green 2X Master Mix (Biosearch Technologies, #30033-1) and primer pairs for wild-type and *Chd4* floxed alleles (Table 1). For Cre-induced excision of loxP-flanked exons that code for the ATPase domain of *Chd4*, a mixture of tamoxifen and β-estradiol was diluted in corn oil. β-estradiol was included to help alleviate the anti-estrogen effects of tamoxifen treatments. Tamoxifen doses for pregnant female mice were adjusted for maternal body weight. Pregnant dams were gavaged with 6.25mg/kg of tamoxifen (Sigma Aldrich, #T5648) and 6.25µg/kg of β-estradiol (Sigma Aldrich, #E8875) daily on embryonic days (E) 8.5- 10.5 to induce Cre activity. For staging timed embryos, the morning that vaginal plugs were observed, pregnant female mice were considered carrying E 0.5 embryos.

Tissue fixation and preparation

Embryos or postnatal pups were sacrificed for inner ear dissection. The temporal bone was identified and removed after bisecting the mouse head and removing the brain. The inner ear was separated from the temporal bone and fixed directly in 4% formaldehyde in 1X PBS overnight at 4°C and washed with 1X PBS overnight at 4°C. Extraneous tissue and bone surrounding the cochlea were removed to obtain the cochlear epithelium and the cochlear duct. Reissner's membrane was removed to expose the sensory epithelium before being processed for immunostaining and *in situ* hybridization. After processing, the cochlea, including spiral ganglion and sensory epithelium, was flat-mounted.

96

97 **Immunohistochemistry**

98 The micro-dissected cochlea tissues fixed in 4% formaldehyde in 1X PBS were permeabilized in wash
99 buffer (1X PBS with 0.1% Triton X-100) for 10 min before being incubated for at least 1 hour in blocking
100 buffer (1X PBS with 0.1% Triton X-100 and 10% normal goat serum) at room temperature. Samples were
101 incubated overnight at 4°C with appropriate primary antibodies diluted in the blocking solution. Samples
102 were then washed with 1X PBS and incubated with the appropriate combinations of DAPI (1 µg/ml), Alexa
103 Fluor 488, Alexa Fluor 568, or Alexa Fluor 647 conjugated secondary antibodies (Thermo Fisher
104 Scientific) for 2 hours at room temperature and washed in 1x PBS before mounting in Prolonged Gold
105 Antifade (Invitrogen, #P36934).

106

107 iMOP cells were fixed in 4% formaldehyde in 1X PBS for 20 minutes at room temperature, incubated in
108 blocking buffer for 1 hour at RT, and incubated overnight with the primary antibodies in blocking buffer at
109 4°C. The next day, cells were washed with 1X PBS and incubated with appropriate combinations of DAPI
110 (1 µg/ml), Alexa Fluor 488, Alexa Fluor 568, or Alexa Fluor 647 conjugated secondary antibodies (Thermo
111 Fisher Scientific) in a blocking buffer for 2 hours at RT. Samples were washed with 1X PBS and mounted
112 in Prolonged Gold Antifade. All antibodies used for immunostaining are listed in Table 2.

113

114 **Single-molecule *in situ* hybridization**

115 Single-molecule fluorescence in situ hybridization (smFISH) was performed using RNAscope (Wang et
116 al., 2012). The RNAscope multiplex fluorescent reagent kit version 2 (Advanced Cell Diagnostics,
117 #323100) was used to detect target RNAs according to the manufacturer's instructions. RNAscope
118 probes are listed in Table 3. Immunohistochemistry was performed after the smFISH protocol to enhance
119 and detect tdTomato protein. Samples were incubated in blocking buffer (1X PBS, 10% goat serum, and
120 0.3% Triton X-100) for 1 hour at room temperature, followed by overnight incubation with rabbit anti-RFP
121 in blocking buffer at 4°C. After incubation with primary antibodies, samples were washed with 1x PBS

122 and incubated with appropriate combinations of DAPI (1 µg/ml) and Alexa Fluor 568 conjugated
123 secondary antibodies (Thermo Fisher Scientific) in a blocking buffer for 2 hours at room temperature.
124 Samples were washed with 1X PBS and mounted in Prolonged Gold Antifade. All antibodies used with
125 RNAscope are listed in Table 2.
126
127 **Fluorescence micrograph acquisition and visualization**
128 Samples were mounted on a 1.5-cover glass and acquired on a Zeiss LSM800 point scanning confocal
129 microscope. Antibody-conjugated fluorophores and tdTomato fluorescent protein were excited using four
130 laser lines (405, 488, 561, and 633nm). 1024X1024 images were acquired using either the 40X (1.4 NA)
131 or 63X (1.4 NA) objective with 1.5-2x digital zoom and 4X Kalmann averaging. The brightness and
132 contrast of images were adjusted and viewed using Zen Blue (Zeiss) or ImageJ.
133
134 **Cell Culture for iMOP cells**
135 Proliferating iMOP cells were cultured in suspension with DMEM/F12 (Gibco, #11320033) containing
136 N21-MAX supplement (R&D Systems, #AR008), 25 µg/ml carbenicillin (Fisher Scientific, # BP2648-1),
137 and 20 ng/ml bFGF (PeproTech, #450-33). Cells were passaged weekly by dissociation using TrypLE
138 Express (Gibco, #12604013), harvested by centrifugation, and resuspended in a fresh medium. To
139 generate iMOP-derived neurons, tissue culture dishes or 12mm coverslips placed in a 24-well plate were
140 coated with 10 µg/mL of poly-D-lysine (PDL; Corning, #354210) for 1 hour at 37°C, then coated overnight
141 with 10 µg/mL of laminin (Gibco, # 23017015) at 37°C, and washed 3 times with 1X PBS before plating
142 cells. Proliferating iMOP cultures were dissociated in TrypLE Express, harvested by centrifugation, and
143 resuspended in neurobasal media (Gibco, #2113049). Resuspended cells were counted using a Moxi
144 counter, and particles between 9-13 µm were considered as cells. Dissociated iMOP cells were plated in
145 PDL-laminin coated culture dishes (1.5-2x10^5 /dish for CUT&Tag) or coverslips in a 24-wells (0.8x10^5
146 cells/well for immunostaining) and cultured in a neurobasal medium containing N21-MAX, 2 mM L-
147 glutamine (Gibco, #25030081), and 1 µM K03861 (Selleck chemicals, #S8100) for neuronal

148 differentiation. On day 3 of culture, the Culture One Supplement (Gibco, A3320201) was added to the
149 media. Fresh medium was added every other day, and neuronal cultures were harvested 7 days after
150 being plated for neuronal differentiation and used for CUT&Tag or immunostaining.
151
152 **CUT&Tag**
153 Cells from proliferating iMOPs and iMOP-derived neurons were harvested and processed using the
154 CUT&Tag-IT Assay Kit (Active Motif, 53160) according to the manufacturer's instructions. Cells were
155 gently dissociated using TrpLE Express and counted and harvested by centrifugation. For each
156 CUT&Tag reaction, 500,000 cells were used. The supernatant from the cell pellet was removed, and cells
157 were resuspended in a wash buffer and placed on ice. Cells were enriched using magnetic Concanavalin
158 A beads and resuspended in an antibody buffer containing a primary antibody to the protein of interest.
159 H3K4me3, p300, CHD4, and IgG antibodies were used for individual samples. All antibodies are listed in
160 Table 2. Two independent samples were used for each antibody condition. Primary antibodies were
161 incubated with the cells for 2 hours at room temperature or overnight at 4°C. All antibodies for CUT&Tag
162 were used at 1:50 dilution. After incubation, the cells were washed and incubated in a buffer containing
163 the assembled pA-Tn5 transposomes and incubated for 1 hour at RT. Cells were washed and processed
164 for tagmentation by incubation in the appropriate buffer for 1 hour at 37°C. A solution containing EDTA,
165 SDS, and proteinase K was added to stop the reaction and solubilize DNA fragments. The solution was
166 placed on a magnetic stand, and the supernatant containing soluble DNA fragments was retained. The
167 DNA solution was purified using a column. The DNA fragments were subjected to PCR amplification and
168 purified using SPRI beads. Libraries generated were quantified and subjected to quality control before
169 performing an Illumina HiSeq 3000 platform (2x150bp). All antibodies used for CUT&Tag are listed in
170 Table 2.
171
172 **Peak calling**

173 Paired-end CUT&Tag reads were aligned to the mm10 genome assembly with bowtie2. Only mapped
174 reads were retained, written to the output, and used for the downstream analysis (Langmead and
175 Salzberg 2012). The bowtie2 SAM output files were converted into BAM files using Samtools (Li,
176 Handsaker et al. 2009). After alignment, sequence reads were scaled using the bamCoverage command
177 in deepTools to remove duplicates and generate normalized bigwig files with reads as Reads Per
178 Kilobase per Million (RPKM) (Ramirez, Dundar et al. 2014). UCSC bigWigToBedGraph utility was used
179 to generate bedgraph files from bigwig files (Kent, Zweig et al. 2010). Peaks were called using Sparse
180 Enrichment Analysis for CUT&RUN (SEACR) (Meers, Tenenbaum et al. 2019). SEACR output bed files
181 from CHD4, H3K4me3, and p300 were generated using CHD4, H3K4me3, and p300 bedgraph files as
182 target files while using IgG bedgraph file as a threshold. BEDtools (Quinlan and Hall 2010) was used to
183 identify consensus peaks with at least 10% reciprocal overlap between replicate samples. Only
184 consensus peaks were used for downstream analysis. CUT&Tag signal tracks were visualized on
185 Integrative Genomic Viewer (IGV) (Robinson, Thorvaldsdottir et al. 2011).
186
187 **Identifying CHD4-bound promoters and enhancers**
188 To perform a global survey of CHD4-bound promoters and enhancers, we first defined CHD4-bound
189 promoters and enhancers in proliferating iMOPs and iMOP-derived neurons. H3K4me3 and p300 were
190 used as promoter and enhancer marks, respectively. CHD4-bound promoters (CHD4+ H3K4me3+) and
191 enhancers (CHD4+ p300+) in iMOPs were identified using BEDtools intersect command. CHD4+
192 H3K4me3+ were identified as regions with at least one base pair overlap between CHD4 and H3K4me3
193 peaks. CHD4+ p300+ regions were defined using the same strategy. SEACR total signals were obtained
194 from the SEACR output file and plotted as box and whisker plots to show the quartiles, mean (circle), and
195 median (line) values. Cell state-specific CHD4-bound promoters or enhancers were identified based on
196 their presence or absence in progenitors and neurons. Genome arithmetic was done using bedtools.
197
198 **Heatmap and profile plots**

199 Heatmaps and profile plots were generated using deepTools. The signal and region files were obtained
200 from the CUT&Tag data. Normalized bigwig files from two replicates were merged using bigwigCompare
201 to acquire average bigwig files and used as signal files. The summit regions corresponding to the
202 maximum SEACR peak signal from CHD4 were used as region files. DeepTools was used to visualize
203 CHD4 and H3K4me3 reads as heatmaps or profile plots. Plots were centered at the summits of CHD4+
204 H3K4me3+, and the average CHD4 or H3K4me3 bigwig signals were plotted +/- 3 kb from the summits.
205 To visualize CHD4 and p300 reads, the summits from CHD4+ p300+ were used as the center, and the
206 average bigwig signals of either CHD4 or p300 bigwig files were plotted within +/- 3kb of the summits.
207

208 **Quantification of heatmap total signals**

209 To quantify CUT&Tag signals displayed in heatmaps, the -outFileNameMatrix option in deepTools was
210 used to retrieve the matrix of signal values underlying the heatmaps. CUT&Tag signals within specified
211 genomic regions were added to obtain the summed signal values. Heatmap signals between progenitors
212 and neurons within the +/- 3kb window were visualized as box and whisker plots.
213

214 **Gene ontology (GO) analysis**

215 To annotate CHD4+ common and neuron-specific promoters and enhancers, ChIPpeakAnno was utilized
216 to determine the closest genes along with the corresponding ensembl gene IDs to those regions (Zhu,
217 Gazin et al. 2010). Unique ensembl gene IDs near CHD4-bound promoters and enhancers were used
218 for GO analysis using DAVID (The Database for Annotation, Visualization and Integrated Discovery)
219 (Huang, Sherman et al. 2009).
220

221 **De Novo Motif Discovery, Comparison and Visualization**

222 Genomic coordinates from SEACR-called CHD4 summits were used to define regions of interest. The
223 regions were converted to GRanges objects. Corresponding DNA sequences were extracted from the
224 *Mus musculus* (mm10) reference genome using the BSgenome.Mmusculus.UCSC.mm10 package. The

225 MEME suite was employed for motif analysis using the memes R package (Bailey, Johnson et al. 2015,
226 Nystrom and McKay 2021). MEME (Multiple Em for Motif Elicitation) was used for *de novo* motif
227 discovery. MEME was configured to identify 20 motifs using the anr (Any Number of Repetitions) model,
228 with motif widths ranging from 6-15 base pairs, searching both forward and reverse complement strands.
229 Position frequency matrices (PFMs) of discovered motifs were normalized to probabilities and visualized
230 as sequence logos using universal motif and ggplot2.
231
232 Discovered *de novo* motifs were compared against known transcription factor binding motifs from the
233 JASPAR2024 CORE database for *Mus musculus* using TomTom. *De novo* motifs, corresponding to the
234 most statistically significant match in JASPAR2024, were based on e-values $< 1 \times 10^{-5}$. The best-
235 matching transcription factor names were used for motif annotation. To assess motif occurrence and
236 distribution around the transcriptional start site (TSS), FIMO (Find Individual Motif Occurrences) was
237 utilized. The regions +/-1kb around the TSS of axon guidance genes harboring CHD4 summits were
238 extracted. FIMO was used to scan these regions for occurrences of all *de novo* motifs. FIMO results were
239 filtered to retain only statistically significant matches with a p-value < 0.05. Motif occurrences with best-
240 match transcription factor names using the TomTom results were mapped and visualized with each axon
241 guidance gene using ggplot2. Individual motif instances were visualized as points relative to the TSS.
242
243 **Statistical analysis**
244 Statistical analyses were performed using either R (R version 4.4.3) or OriginPro (Origin Lab) for normally
245 distributed data. The means of data were presented and subjected to an unpaired two-tailed Student's t-
246 test to determine statistical significance and provide a p-value. Results with p values <0.05 were
247 considered statistically significant. Unless noted, the p values are defined as *p<0.05, **p<0.01, and
248 ***p<0.001. Bar graphs display the means ± standard error of the mean (SEM), and violin plots show the
249 distribution and mean of the data points. The numbers displayed in the text indicated the means ± SEM.
250

Data for CUT&Tag and RNAscope were determined not to be normally distributed using the Shapiro-Wilks normality test. The median was presented and subjected to a non-parametric Wilcoxon rank-sum test to determine whether the paired samples differed statistically. Analysis of the data was performed in R. The normalized read counts (RPKM) from CUT&Tag were displayed as box and whisker plots to show the quartiles, means, and medians. Horizontal lines within the box denoted the median values, while the circles represented the means. The number displayed in the text indicates the median ± standard deviation (sd) of CUT&Tag signals for box and whisker plots. The RNAscope images were counted to determine the distribution, mean, and median of puncta counts per cell. Unless noted, the p-values from the Wilcoxon rank-sum test were defined as $p < 0.05$ to be significant. The numbers displayed indicate the median ± sd in the text and the median of puncta counts in the figure. The variance was calculated as the sum of the squared difference between puncta counts and the sample mean, divided by the sample size minus one. Levene's test for the homogeneity of variance was used to determine whether the variances were statistically significant. The p-values from Levene's test were defined as $p<0.05$ to be significant.

266 **Results**

267

268 **CHD4 expression in cochlear cell types**

269

270 SGNs are bipolar and pseudounipolar neurons of the cochlea. The somas of SGNs reside within the
271 modiolus and extend a peripheral process through Rosenthal's canal towards the sensory hair cells, while
272 a central process from the cell soma projects to the cochlear nucleus in the brainstem. SGNs are broadly
273 classified as type I and type II neurons. Type I SGNs are the primary afferents that consist of 90-95% of
274 the neuronal population in the spiral ganglion. Type I SGNs are myelinated and form a single synaptic
275 bouton with inner hair cells that reside in the organ of Corti (Fig. 1A). Multiple type I SGNs synapse along
276 the basolateral surface of inner hair cells (IHCs) (Liberman 1982). Type I SGNs differ in sensitivity to
277 sound and spontaneous firing rate (SR), as revealed by single-fiber recordings in the cat auditory nerve
278 (Kiang, Pfeiffer et al. 1965). The relationship between threshold and SR predicted three distinct
279 populations of low, medium, and high SR neurons (Liberman 1978). These three subtypes are present
280 irrespective of tonotopic position along the length of the cochlea (Borg, Engstrom et al. 1988, Schmiedt
281 1989, Winter, Robertson et al. 1990, el Barbary 1991, Taberner and Liberman 2005, Shrestha, Chia et
282 al. 2018, Sun, Wang et al. 2022). SGNs display different receptors and ion channel regulators that shape
283 their sensitivity and SR. The molecular heterogeneity correlated with the differences in
284 electrophysiological properties of these neurons (Adamson, Reid et al. 2002, Chen, Xue et al. 2011, Liu,
285 Manis et al. 2014, Liu and Davis 2014).

286

287 Type II afferent neurons account for 5–10% of the neuronal population (Spoendlin 1972, Ruggero, Santi
288 et al. 1982). Type II SGNs are pseudounipolar and unmyelinated neurons that turn towards the cochlear
289 base (Zhang and Coate 2017). During outgrowth, Type II SGN peripheral axons turn after the growth
290 cone passes between the basolateral surfaces of the inner pillar cells. Turning occurs among the outer
291 pillar and Deiters' cells as they are directed towards the cochlear base (Fig. 1A). This process is mediated

292 by planar cell polarity complexes formed between cochlear-supporting cells for non-cell autonomous
293 regulation of axon pathfinding (Ghimire, Ratzan et al. 2018, Ghimire and Deans 2019). The peripheral
294 axons then gradually ascend apically toward the outer hair cells (OHCs) after turning to join other type II
295 axons in one of three outer spiral bundles that extend along the length of the cochlea (Fig. 1B). Each
296 type II afferent neuron innervates multiple OHCs from the same row, with individual OHC receiving an
297 *en-passant* contact from a type II afferent neuron (Zhang and Coate 2017).
298
299 To determine the expression of CHD4, neonatal cochleae from embryonic day (E) 18.5 embryos were
300 harvested. At this point, type I and type II SGNs are morphologically distinct, and the neurites have
301 extended toward IHCs and OHCs, respectively. The cochleae were subjected to immunostaining with
302 CHD4 and TUBB3 antibodies to mark the presence of type I and type II SGNs along with CHD4 (Fig.
303 1C). The fiber tracks from their innervation pattern can identify the type of SGNs. As previously described,
304 many different cell types within the organ of Corti, including IHCs and OHCs, express CHD4 (Layman,
305 Sauceda et al. 2013). We confirmed the presence of CHD4 in MYO7A labeled hair cells (Fig. 1D). CHD4
306 was also expressed in the nuclei of inner pillar, outer pillar and the three rows of Dieter cells and other
307 supporting cells (Fig. 1E). Finally, CHD4 was strongly expressed in the nucleus of spiral ganglion neurons
308 (SGNs) marked by TUBB3 in the modiolus (Fig. 1F). Expression of CHD4 was present in all TUBB3-
309 marked SGNs. The presence of *Chd4* transcripts in developing SGNs (Lu, Appler et al. 2011) and our
310 results suggest that CHD4 may function in SGNs during inner ear development.
311
312 **Deletion of *Chd4* in SGNs**
313
314 CHD4 is present in many inner ear cell types, and mutations that inactivate CHD4 chromatin remodeling
315 activity may contribute to improper development or dysfunction of multiple inner ear cell types. Since
316 SGNs highly express CHD4, we wanted to delineate how CHD4 ablation in SGNs contributes to the
317 development of the cochlea and hearing loss. Targeted ablation of CHD4 from SGNs using a

318 Neurogenin1 (Ngn1) CreER^{T2} *Chd4*$^{flox/flox}$ animal was accomplished. The Ngn1 CreER^{T2} *Chd4*$^{flox/flox}$
319 animals contain two copies of the *Chd4* conditional knockout (cKO) allele, where loxP sites flanked exons
320 that code for the ATPase domain required for nucleosome repositioning (Williams, Naito et al. 2004). The
321 Ngn1 CreER^{T2} transgenes harbor a tamoxifen-inducible Cre expressed in neurosensory progenitors and
322 can be used for genetic manipulations in SGNs (Koundakjian, Appler et al. 2007). Tamoxifen
323 administration to Ngn1 CreER^{T2} animals allowed Cre-mediated excision of loxP-flanked DNA in inner ear
324 neurosensory progenitors that become SGNs (Koundakjian, Appler et al. 2007, Raft, Koundakjian et al.
325 2007). To ensure Cre activity was present in the intended cell types, *Chd4*$^{flox/flox}$ Ngn1 CreER^{T2} were
326 crossed to the Ai9 tdTomato reporter (Madisen, Zwingman et al. 2010). In the triple transgenic animals,
327 tamoxifen administration allows Cre-activated Ai9 tdTomato reporter expression and enables
328 fluorescence visualization of SGN cell bodies and axonal projections while simultaneously deleting *Chd4*
329 (Fig. 2A). Control (Ngn1 CreER^{T2}; Ai9) and *Chd4* cKO (Ngn1 CreER^{T2}; *Chd4*$^{flox/flox}$; Ai9) lines were
330 generated. Timed matings from either control or *Chd4* cKO lines produced pregnant dams that were
331 administered with tamoxifen to produce embryos for analysis.
332
333 During inner ear development, delaminating otic progenitors around E9 from the proneurosensory
334 domain of the otic vesicle coalesce to form the cochlear-vestibular ganglion (CVG). As development
335 progresses, the CVG neurons segregate to create the spiral ganglion. A population of neurons exits the
336 cell cycle and terminally differentiates at the base and middle of the cochlea starting from E9.5-10.5. Most
337 SGNs exit the cell cycle around E11.5 in the middle and base of the cochlea, while cells in the apex exit
338 the cell cycle at E12.5. After exiting the cell cycle, peripheral projections from SGNs extend toward the
339 sensory epithelium of the cochlea. At E12.5, SGN projections begin to extend beyond the spiral ganglion
340 border. At E15.5, SGN peripheral axon outgrowth continues along the length of the cochlea. Type I SGNs
341 form radial fiber bundles that undergo fasciculation. Between E15.5-18.5, type I-like SGN processes
342 show extensive branching around and beyond the inner hair cells. The neurites are subsequently refined
343 by retracting from the outer hair cell region (Appler and Goodrich 2011, Coate, Spita et al. 2015). Type II

344 SGNs are notably distinct from Type I SGNs by E16.5 based on their peripheral projections ending at the
345 outer hair cell region (Bruce, Kingsley et al. 1997). The Ngn1 CreER^{T2} animals with a reporter can mark
346 delaminating neurosensory progenitors that develop into type I and type II SGNs at the aforementioned
347 developmental stages (Koundakjian, Appler et al. 2007).
348
349 *Chd4* was deleted by administering daily tamoxifen doses to pregnant dams between E8.5-10.5. During
350 this time, *Chd4* was deleted from neurosensory progenitors that give rise to SGNs. Labeled cells were
351 used to study the consequences of *Chd4* ablation in developing type I and type II SGNs. E18.5 embryos
352 were harvested from pregnant dams after tamoxifen treatment. Although some embryos survived, many
353 resorptions occurred perinatally after tamoxifen administration. Quantification and comparison of
354 resorbed embryos from control and *Chd4* cKO dams suggest a significant reduction in viability of *Chd4*
355 cKO embryos (Fig. S1A). Quantifying the number of surviving embryos from individual litters obtained
356 from pregnant dams showed a statistically significant reduction in embryo viability after *Chd4* deletion
357 (Fig. S1B). Cre recombinase expression in the Ngn1 CreERT^2 is not limited to the inner ear but can also
358 be observed throughout the central nervous system (Kim, Hori et al. 2011). These findings suggest
359 deleting *Chd4* in other cell types may decrease viability in the *Chd4* cKO embryos.
360
361 Cochleae were harvested and used for immunostaining from the remaining embryos. To ensure that the
362 genetic deletion of *Chd4* lacked protein, immunofluorescence labeling of the CHD4 protein was done.
363 TUBB3 immunofluorescence was used to identify SGNs. The tdTomato fluorescence suggested that Cre
364 activity was present in TUBB3-marked SGNs in both control and *Chd4* cKO cochleae samples. Even
365 though SGNs were present in the cochleae, only the CHD4 signal was seen in controls and not in *Chd4*
366 cKO cochleae (Fig. 2B). These results showed that CHD4 protein was absent in the *Chd4* cKO cochlea
367 after tamoxifen treatment and that CHD4 was not essential for SGN viability at embryonic and neonatal
368 stages. In E18.5 embryonic cochlea, an increase in the number of tdTomato+ and TUBB3-negative cells
369 was observed in *Chd4* cKO (Fig. 2C). To quantify the percentage of the marked cell populations, SGNs

370 from dissected cochlea were divided into three regions corresponding to the apex, middle, and base of
371 the cochleae. In controls, a low percentage of cells lacking TUBB3 but expressing tdTomato was
372 observed (apex: 6.81 ± 1.69%, middle: 4.07 ± 1.94%, base: 3.95 ± 1.74%), while in *Chd4* cKO cochlea,
373 increased percentages of these cells were observed along the length of the cochleae (apex: 12.06 ±
374 2.25%, middle: 8.73 ± 0.91%, base: 7.82 ± 1.29%; apex, $p < 0.14$, middle, $p < 0.10$; base, $p < 0.15$) (Fig.
375 2D). The percentage of TUBB3 labeled SGNs marked by tdTomato allowed us to confirm the efficiency
376 of Cre-mediated activity in these cells. In control embryos, Cre activity was observed in almost all SGNs
377 with a slight decrease in labeled cells at the apex (apex: 89.86 ± 3.56%, middle: 97.09 ± 1.48%, base:
378 98.97 ± 0.36%). Since development proceeds in a base-to-apex manner, the decreased percentage of
379 tdTomato-marked cells located at the apical region of the cochlea was likely due to a small population of
380 late-born neurons that were not exposed to tamoxifen during the time window of administration. *Chd4*
381 cKO displayed similar percentages of tdTomato marked cells (apex: 84.35 ± 2.99%, middle: 95.71 ±
382 1.96%, base: 98.91 ± 0.2%; apex $p < 0.30$; middle $p < 0.60$; base, $p < 0.90$). The percentages of
383 tdTomato+TUBB3+ cells from control and *Chd4* cKO cochlea were not statistically different (Fig. 2E).
384 The numbers of tdTomato+ cells from *Chd4* cKO were not significantly different from control (44.22 ±
385 0.41% for control, 49.70 ± 2.32% for *Chd4* cKO, $p < 0.08$) (Fig. 2F). These results suggest that tamoxifen
386 induced Cre recombination was efficient along the entire length of the cochlea and was similar between
387 control and *Chd4* cKO cochleae.
388
389 ***Chd4* cKO cochleae displayed altered fasciculation of radial fiber bundles**
390
391 Deletion of *Chd4* in embryos showed that SGNs were present and in comparable percentages as
392 controls. Although *Chd4* may not dramatically affect the viability or early developmental stages, we
393 wanted to determine whether loss of *Chd4* showed discernible differences at later stages. Post-mitotic
394 neurons from the spiral ganglion extend neurites towards inner and outer hair cells, starting from the base
395 to the apex. Type I and type II SGNs target IHCs and OHCs, respectively. Type I and type II SGN fiber

396 tracks and innervation patterns were marked by performing whole mount TUBB3 immunostaining using
397 cochleae from control and *Chd4* cKO (Fig. 3A).
398
399 The peripheral axons of type I SGNs extend from the soma to form a radial bundle. The type I SGN fibers
400 fasciculate, the terminals extensively branch around the inner spiral plexus (ISP) and retract from the
401 outer hair cell region back into the IHC region (Fig. 3B). In *Chd4* cKO cochleae, radial fibers were less
402 compact and showed wider nerve fascicles. The area between the fiber bundles was identified by
403 converting TUBB3 immunofluorescent images to black-and-white binary images. The white regions
404 between fiber bundles and the total area from the SGN soma to the sensory epithelium were determined
405 from images taken along the length of the cochlea (Fig. 3C). The percent area unoccupied by radial fibers
406 relative to the total area was calculated and used as a metric for fasciculation (Fig. 3D). The average
407 percentage of unoccupied space in *Chd4* cKO cochleae was significantly decreased (33.19 ± 2.59% for
408 control and 25.12 ± 1.28% for *Chd4* cKO, $p < 0.05$). The result suggested that the radial fibers from *Chd4*
409 cKO cochleae covered more area and thus were wider than controls (Fig. 3E). The fiber bundles were
410 counted in control and *Chd4* cKO cochleae to determine the fascicle numbers in the inner spiral plexus
411 (ISP) (Fig. 3F). The ISP consists of the region where radial fibers extend from the soma through
412 the *habenula perforata* to innervate the IHC (Fig. 1). The average number of fascicles in ISP per inner
413 radial bundle increased significantly in *Chd4* cKO cochleae (4.48 ± 0.16 bundles for control and 6.54 ±
414 0.67 bundles for *Chd4* cKO, $p < 0.01$) (Fig. 3G). These results show an increased number of inner radial
415 fiber bundles and less compact bundling of the nerve fiber.
416
417 ***Chd4* cKO cochleae display improper turning of type II fibers**
418
419 Type II SGNs constitute only 5-10% of the total SGN population, but their axonal projections are spatially
420 distinct from type I SGNs. During development, their peripheral processes cross the tunnel of Corti into
421 the outer hair cell region, where the axons make a right-angle turn and travel from the base of the cochlea

422 towards the apex to make *en passant* synapses with outer hair cells. The outer spiral fibers are the
423 bundled neurites from type II SGNs that extend along the OHC region. Each OHC is innervated by 2-5
424 type II SGNs (Huang, Barclay et al. 2012, Martinez-Monedero, Liu et al. 2016). To look at the outer spiral
425 fiber tracks, TUBB3-labeled neurons from whole mount cochleae were used for analysis (Fig. 4A). The
426 magnified images of outer spiral fibers usually display three main fiber tracks that travel along individual
427 rows of outer hair cells with intermittent fibers crossing these tracks. To show quantitative differences
428 between the outer spiral tracks, intensity profiles from control and *Chd4* cKO cochleae images spanning
429 the outer hair cell region were taken (Fig. 4B). Measurements of the intensity profile show different peaks
430 corresponding to the presence of fibers. The intensity profile plot showed three prominent peaks in the
431 control cochlea (black). In contrast, *Chd4* cKO cochlea (red) displayed additional peaks (Fig. 4C). The
432 data suggested that there are type II SGN fibers or individual axons that detract from the outer fiber tracts
433 (Fig. 4C). Each major peak corresponds to an outer spiral bundle consisting of multiple fibers. The
434 appearance of the minor peaks within a major peak corresponds to the increased dispersion of the fibers
435 within an outer spiral fiber. The number of distinct fibers observed by fluorescent microscopy in the outer
436 hair cell region was counted and normalized based on the area to validate the altered axon paths. Similar
437 to the intensity profile, the number of fibers in the OHC area increased in *Chd4* cKO samples compared
438 to controls (13.98 ± 0.73 fibers for controls and 17.64 ± 0.78 fibers for *Chd4* cKO, $p < 0.03$) (Fig. 4D).
439 These results suggest aberrant bundling of the outer spiral fibers after *Chd4* ablation in SGNs.
440
441 We also noticed the aberrant turning of the outer spiral fiber tracks. Turning of the type II SGN fibers
442 usually occurs near the inner pillar cell (IPC), outer pillar cell (OPC) or Dieter cell (DC) region. Confocal
443 micrographs were acquired below the outer hair cell layer up to the sensory epithelium to visualize the
444 fiber turning. Individual fibers from control cochleae turned towards the base of the cochlea before joining
445 one of the three outer spiral fiber tracks. In contrast, the *Chd4* cKO cochleae showed fibers turning in the
446 opposite direction (Fig. 4E, yellow arrows). Incorrectly turned type II fibers were quantified in control and
447 *Chd4* cKO cochleae (Fig. 4F). These data showed that the deletion of *Chd4* increases the incorrect

448 turning of type II SGNs in the outer spiral fibers (0.12 ± 0.06 fibers for control and 1.93 ± 0.14 fibers for
449 *Chd4* cKO, $p < 2.83 \times 10^{-4}$). Turning of the fibers has previously been shown to require cell signals from
450 supporting cells (Ghimire, Ratzan et al. 2018, Ghimire and Deans 2019, Deans 2022). To ensure that
451 supporting cells in the organ of Corti were present and not indirectly affected by *Chd4* deletion,
452 immunostaining for both hair cells and supporting cells, using MYO7A and SOX2, was performed in
453 control and *Chd4* cKO cochlea. A single row of inner hair cells and three rows of outer hair cells were
454 present in both samples. Moreover, SOX2-labeled supporting cells showed the presence of organized
455 supporting cells residing below hair cells (Fig. S2). These results suggest that *Chd4* deletion in SGNs
456 affects the turning of type II SGNs in a cell-autonomous manner.
457
458 ***Chd4* cKO cochleae display aberrant basal to apical axon path towards outer hair cells**
459
460 Alterations in axon paths could also be due to how fibers exit Rosenthal's canal and ascend toward the
461 outer hair cells. To determine if this is the case, reconstructed confocal images of MYO7A-labeled hair
462 cells provide a landmark for the terminal destination of axons. We observed that many type II tracks take
463 a more circuitous route toward the OHCs because the fibers initially descend basally and migrate further
464 away from the soma of outer hair cells (Fig. 4G). The distances were obtained from the bottom of
465 individual OHC somas to the furthest detectable axon fibers directly below. The measurements were
466 used to quantify the aberrant axon path (Fig. 4H). The measurements showed an increase in the average
467 distance of the fibers to the bottom of hair cells in *Chd4* cKO cochleae (17.84 ± 0.66μm for control and
468 29.87 ± 3.74μm for *Chd4* cKO, $p < 0.03$). The increased distance measured in *Chd4* cKO cochleae
469 suggested that outer spiral fibers do not properly ascend from Rosenthal's canal towards the outer hair
470 cells (Fig. 4I). Many of these changes in fiber tracks and innervation patterns observed both in type I and
471 type II SGNs are reminiscent of axon guidance defects. Although these findings implicate CHD4 in axon
472 pathfinding, the molecular targets for CHD4 in SGNs are unknown.
473

474 **Enrichment of CHD4 at cis-regulatory regions of *Eph* and *Ephrin* genes**

475

476 CHD4 function is cell-type dependent, and its chromatin activity likely alters a unique repertoire of cis-
477 regulatory elements in SGNs to control gene expression. A significant hurdle is identifying high-
478 confidence occupancy sites for CHD4 in SGNs by chromatin immunoprecipitation followed by deep
479 sequencing (ChIP-seq) or Cleavage Under Targets & Tagmentation (CUT&Tag). The inability to identify
480 these high-confidence sites in SGNs is partly due to the large number of cells required for the
481 experiments. Instead of primary SGNs, we used immortalized multipotent otic progenitor (iMOP)-derived
482 neurons to determine genome-wide binding sites for CHD4 to identify potential target genes.
483 Immortalized multipotent otic progenitors (iMOP) derived neurons are highly similar at the transcriptome
484 level to primary otic progenitors from which they were derived and can differentiate into cells that display
485 bipolar and pseudounipolar morphology similar to SGNs (Kwan, Shen et al. 2015).

486

487 Immunostaining confirmed the presence of CHD4 in the nucleus of proliferating iMOPs and TUBB3-
488 expressing iMOP-derived neurons (Fig. 5A). To identify genome-wide CHD4 binding sites, CUT&Tag
489 was performed using CHD4 antibodies on proliferating iMOP and iMOP-derived neurons. CHD4
490 occupancy is cell-type specific and is recruited to active promoters and enhancers to repress transcription
491 (Yang, Yamada et al. 2016, Yoshida, Hu et al. 2019). We used the H3K4me3 and p300 marks as genomic
492 landmarks for promoters and enhancers. Sparse Enrichment Analysis for CUT&RUN (SEACR) identified
493 regions of high-confidence enrichment, known as peaks, from all CUT&Tag sequence reads (Meers,
494 Bryson et al. 2019). We compared CHD4 peaks to H3K4me3 and p300-bound regions. The heatmaps
495 provided a distribution of the reads within a +/- 3 kb window. The profile plots allowed us to evaluate the
496 read density over the same genomic regions qualitatively. We identified CHD4+ H3K4me3+ regions
497 based on the occupancy of CHD4 and H3K4me3 peaks in proliferating iMOP cells and iMOP-derived
498 neurons (Fig. S3B). The CHD4+ H3K4me3+ regions corresponded to CHD4-bound promoters. Similarly,
499 we defined CHD4+ p300+ regions in proliferating iMOP cells and iMOP-derived neurons (Fig. S3C). The

500 CHD4+ p300+ regions corresponded to CHD4-bound enhancers. From the profile plots, we noticed that
501 the CHD4 signal increased in iMOP-derived neurons compared to proliferating iMOPs at both promoters
502 and enhancers. We quantified and compared the CHD4 total signals at CHD4+ H3K4me3+ promoters
503 and CHD4+ p300+ enhancers between proliferating iMOP and iMOP-derived neurons. We showed that
504 at CHD4-bound promoters, CHD4 total signals increased 2.80-fold in iMOP-derived neurons (57,811.40
505 ± 65,983.40 RPKM) compared to proliferating iMOPs (20,684.90 ± 25,408.89 RPKM, $p < 2.20 \times 10^{-16}$).
506 At CHD4-bound enhancers, we found a 4.65-fold increase of CHD4 total signal in iMOP-derived neurons
507 (134,027.50 ± 102,349.97 RPKM) compared to proliferating iMOPs (28,837.65 ± 29,014.11 RPKM, $p <$
508 2.20×10^{-16}) (Fig. 5B). The results suggest that increased enrichment of CHD4 at cis-regulatory regions
509 in iMOP-derived neurons may regulate gene expression during neuronal differentiation.
510
511 To investigate the involvement of CHD4 during neuronal differentiation, we identified CHD4 binding sites
512 present in iMOP-derived neurons. We did this by comparing CHD4-bound regions between proliferating
513 iMOPs and iMOP-derived neurons. At CHD4+ H3K4me3+ promoters, we found 982 progenitor-specific,
514 168 neuron-specific, and 1,092 common promoters in both proliferating iMOPs and iMOP-derived
515 neurons. At CHD4+ p300+ enhancers, we identified 2,106 progenitor-specific, 223 neuron-specific, and
516 750 common enhancers (Fig. 5C). We focused on common and neuron-specific regions since CHD4
517 activity may exert epigenetic changes at these sites during neuronal differentiation. We generated
518 heatmaps and profile plots for each of the regions. At common promoters, we observed a 1.20-fold
519 increase of H3K4me3 in iMOP-derived neurons (25,871.92 ± 12,797.10 RPKM) compared to proliferating
520 iMOPs (21,550.36 ± 9,015.10 RPKM, $p < 3.67 \times 10^{-23}$) and a 2.28-fold increase in CHD4 in iMOP-derived
521 neurons (5,407.49 ± 2,955.04 RPKM) compared to proliferating iMOPs (2,371.49 ± 1573.27 RPKM, $p <$
522 3.46×10^{-282}). At neuron-specific promoters, a 1.31-fold increase in H3K4me3 (proliferating iMOP
523 17,105.85 ± 10,709.21 RPKM, iMOP-derived neurons 22,411.04 ± 14,180.57 RPKM, $p < 3.87 \times 10^{-7}$) and
524 3.30-fold increase in CHD4 (proliferating iMOP 1,397.09 ± 2,617.01 RPKM, iMOP-derived neuron

525 4,608.37 ± 3,173.27 RPKM, $p < 4.22 \times 10^{-45}$) was observed in iMOP-derived neurons (Fig. 5D). All
526 observed increases in H3K4me3 and CHD4 were statistically significant.
527
528 We performed a similar analysis for enhancers. The heatmaps and profile plots showed a distribution of
529 p300 and CHD4 centered at common and neuron-specific enhancers. A 3.37-fold increase in p300
530 (proliferating iMOP = 2,838.41 ± 1,713.93 RPKM, iMOP-derived neuron = 9,578.39 ± 4531.32 RPKM, p
531 $< 5.92 \times 10^{-223}$) was observed at common enhancers. CHD4 displayed a 2.84-fold increase in signal from
532 iMOP-derived neurons (proliferating iMOP 4,068.79 ± 2,542.82 RPKM, iMOP-derived neuron 11,559.34
533 ± 4,647.43 RPKM, $p < 9.30 \times 10^{-210}$). At common and neuron-specific enhancers, a statistically significant
534 increase in signal was detected for p300 and CHD4 in iMOP-derived neurons compared to proliferating
535 iMOPs (Fig. 5E). The results suggest that CHD4 was significantly enriched at specific promoters and
536 enhancers during neuronal differentiation. The increased occupancy likely alters the chromatin state of
537 these cis-regulatory regions to regulate transcription.
538
539 To gain biological insights into CHD4 targets, genes near common and neuron-specific regulatory
540 elements were identified (Table S1). The identified target genes were used for gene ontology analysis.
541 Gene ontology (GO) analysis revealed function in chromatin organization ($p < 5.10 \times 10^{-14}$), which is
542 consistent with the predicted cellular process of CHD4 in inner ear neurons. Other biological processes
543 such as ephrin receptor signaling ($p < 4.90 \times 10^{-5}$), axon guidance ($p < 2.00 \times 10^{-13}$), semaphorin-plexin
544 signaling during axon guidance ($p < 2.70 \times 10^{-2}$), axonal fasciculation ($p < 1.60 \times 10^{-2}$), and axonogenesis
545 ($p < 1.60 \times 10^{-14}$) were some of the notable cellular processes (Fig. S3A). The GO analysis suggested
546 that CHD4 gene targets may regulate processes involved in axon pathfinding, including ephrin receptor
547 signaling. We identified *Epha4*, *Epha7*, *Ephb3*, *Efna3*, *Efna4*, *Efnb2*, *Efna5*, *Efnb1*, *Ephb2,* and other
548 axon guidance genes as candidates based on their proximity to CHD4-bound promoter and enhancer
549 regions (Table S1). Ephrin signaling pathways are essential in guiding SGN peripheral axons. We
550 focused on *Epha4*, *Epha7*, and *Efnb2* because these genes have previously been implicated to function

551 in the inner ear (Coate, Raft et al. 2012, Defourny, Poirrier et al. 2013, Kim, Ibrahim et al. 2016, Petitpre,
552 Wu et al. 2018, Sanders and Kelley 2022). At *Epha4* and *Epha7*, CHD4, and H3K4me3 peaks were
553 observed near the transcriptional start site. We also observed an increase in CHD4 and p300 in iMOP-
554 derived neurons at multiple intronic regions, a region upstream at *Epha4* and a singular downstream site
555 at *Epha7* (Fig. 5F). A similar observation was noted for *Efnb2* (Fig. S3D), where CHD4 was enriched at
556 the H3K4me3 marked promoter along with increased CHD4 and p300 signals at a downstream enhancer
557 region. In contrast, CHD4 was not observed at the transcriptional start site of *Calb2*, a non-target gene
558 (Fig. S3E). These results imply that CHD4 binding to promoters and enhancers may control the
559 transcription of *Eph* receptors and *Efn* ligands. The altered expression of these genes may be pertinent
560 to the axon guidance deficits seen in the *Chd4* cKO cochleae.
561

562 **DNA binding motifs near Eph receptor and ephrin ligand genes**

563 Although CHD4 may regulate the epigenetic state at cis-regulatory regions of axon guidance genes, it
564 does not have a direct DNA-binding motif (Laureano, Kim et al. 2023). We wanted to identify potential
565 transcription factors that may regulate the expression of *Eph* and *Efn* genes. To gain insight into the
566 transcriptional regulation, *de novo* DNA motif discovery on CHD4-enriched regions was done to identify
567 potential TF binding sites. Starting with SEACR-defined summits obtained from CHD4 peaks, we first
568 identified 1,095 sites within ±1 kb of TSS (Fig. S4A). Next, we focused on CHD4 binding within ±1 kb of
569 TSS at axon guidance genes to identify 16 sites (Fig. S4B). *De novo* motif discovery was done to identify
570 motif consensus sequences. To annotate the *de novo* motifs, they were compared to known TF motifs,
571 and statistically significant matches were displayed on a heatmap with their corresponding p values (Fig.
572 S4C). Motif occurrences and Information Content Scores (ICS), a conservation metric, were determined
573 and plotted (Fig. S4D). Motif occurrences and relative positions to the TSS were shown for each axon
574 guidance gene (Fig. S5A). The probability of base pair composition from identified motifs was visualized
575 using sequence logos (Fig. S5B).

576 We identified distinct combinations of TF motifs for *Epha4*, *Epha7*, and *Efnb2*, genes previously
577 implicated in axon guidance in the cochlea. *Epha4* contained *Stat2* (Signal transducer and activator of
578 transcription 2), two *Lhx3 (*LIM homeobox 3), and an *Ar* (Androgen Receptor) motif. *Epha7* harbored
579 *Stat2*, *Plagl1* (Pleiomorphic Adenoma Gene-like 1), and *Hnf1A* (Hepatic Nuclear Factor 1 Alpha) motifs.
580 *Efnb2* displayed a single *Ar* motif. These motifs were displayed as sequence logos (Fig. 6A). This
581 analysis revealed potential TFs that may function with CHD4 to regulate *Epha4*, *Epha7*, and *Efnb2*
582 transcription.

583

584 **Chd4 cKO showed increased *Eph* and *Efn* mRNA levels in SGNs**

585

586 To validate if deletion of CHD4 in SGNs affects the level of ephrin molecules, cochleae from control and
587 *Chd4* cKO were subjected to fluorescence *in situ* hybridization (RNAscope). We used *Calb2* (*Calbindin2*)
588 transcripts as a marker for SGNs and as a gene unaffected by CHD4. We simultaneously probed for the
589 *Eph* or *Efn* transcripts. TUBB3 immunolabeling was combined with RNAscope to demarcate SGNs for
590 quantification in control (Fig. 6B) and *Chd4* conditional knockout (Fig. 6C). The soma of individual TUBB3-
591 marked SGNs were used to determine regions of interest for puncta quantification to determine the
592 relative number of mRNA molecules in each neuron (Fig. 6D).

593

594 The *Calb2* puncta were quantified and there was no significant difference observed in *Calb2* transcript
595 levels between *Chd4* cKO (8 ± 5.51 *Calb2* puncta/cell) and control (9 ± 6.16 *Calb2* puncta/cell, $p < 0.13$)
596 (Fig. 6E). The distribution of *Calb2* puncta counts per cell was visualized as a histogram to display the
597 number of cells with specified *Calb2* puncta/cell. This histogram was transformed into a density plot to
598 illustrate the probability distribution of puncta counts per cell. The variance was calculated using the
599 density plot. As observed, the density plots for both control and *Chd4* cKO SGNs were not appreciably

600 different, and the variance of *Calb2* transcripts showed a slight 1.25-fold decrease in *Chd4* cKO (σ^2 =
601 30.36) compared to the control (σ^2 = 37.93, $p < 0.04$) (Fig. 6E).
602
603 In contrast, the average number of *Epha4* puncta in the SGN population increased in *Chd4* cKO (13 ±
604 6.29 puncta/cell) compared to the control (7 ± 4.00 puncta/cell, $p < 1.74 \times 10^{-39}$) and was statistically
605 significant. By transforming the distribution of the *Epha4* puncta/cell into a density plot, we observed a
606 2.47-fold increase in the variance of *Epha4* transcripts in *Chd4* cKO (σ^2 = 39.51) compared to control
607 SGNs (σ^2 = 16.00, $p < 2.27 \times 10^{-14}$). The non-overlapping regions in the density estimates reflect the
608 increased probability of cells with higher *Epha4* transcript levels in the absence of *Chd4* (Fig. 6F). The
609 results suggest that deletion of *Chd4* in SGNs increases *Epha4* in a subpopulation of SGNs. In contrast
610 to *Epha4*, the decreased variance in *Calb2* puncta/cell may be caused by a CHD4-independent
611 mechanism or an indirect effect of *Chd4* deletion.
612
613 To further validate additional targets of axon guidance genes, we performed RNAscope on the two other
614 members of the Ephrin receptor and ephrin ligand family, *Epha7* and *Efnb2,* that displayed CHD4 binding
615 at their promoters. *Epha7* puncta in SGNs were significantly increased in *Chd4* cKO (18 ± 7.55 *Epha7*
616 puncta/cell) compared to the control (12 ± 5.67 *Epha7* puncta/cell, $p < 2.48 \times 10^{-45}$) and the variance of
617 *Epha7* transcripts showed a 1.77-fold increase in *Chd4* cKO (σ^2 = 56.95) compared to the control SGNs
618 (σ^2 =32.19, $p < 8.29 \times 10^{-11}$) (Fig. 6G). A similar increase in *Efnb2* puncta *was* observed in *Chd4* cKO (23
619 ± 9.31 puncta/cell*)* compared to control (16 ± 8.22 puncta/cell, $p < 7.33 \times 10^{-24}$). A 1.28-fold increase in
620 the *Efnb2* variance was observed in *Chd4* cKO (σ^2 = 86.76) compared to control SGNs (σ^2 =67.57, p <
621 0.04) (Fig. 6H). The results suggest an increased likelihood of *Chd4* cKO SGNs harboring more *Epha4*,
622 *Epha7*, and *Efnb2* transcripts, due to the loss of CHD4. The data indicate that CHD4 normally represses
623 transcription of a subset of Eph receptor and ephrin ligand genes. Ablation of *Chd4* increases transcript
624 levels of the axon guidance genes in a proportion of cells, resulting in aberrant peripheral axon
625 pathfinding.

626 **Discussion**

627

628 CHD4 is expressed in cochlear supporting cells and hair cells from E18 to P21 (Layman, Sauceda et al.
629 2013). Gene expression analysis showed that *Chd4* transcripts are present and changing in developing
630 murine SGNs from E12 to P15 (Lu, Appler et al. 2011). *De novo* pathogenic variants of *CHD4* correlate
631 to SIHIWES, an autosomal dominant neurodevelopmental disorder**.** Patients with pathogenic variants of
632 CHD4 show variable symptoms, and many have hearing loss (Sifrim, Hitz et al. 2016, Weiss, Terhal et
633 al. 2016). CHD4 has a core ATPase SWI/SNF domain that hydrolyzes ATP and converts it into chromatin
634 repositioning activity. Some pathogenic mutations result in CHD4 protein with reduced chromatin
635 remodeling activity (Weiss, Lazar et al. 2020). To clarify the contribution of CHD4 in SGNs, we employed
636 a conditional knockout mouse model that allows Cre-dependent inducible deletion of the exons coding
637 for the ATPase domain of CHD4 in SGNs. The conditional knockout mouse allowed us to separate the
638 CHD4 function from other inner ear cell types, such as hair cells and supporting cells. Our current results
639 implicate a cell-autonomous role for CHD4 in the pathfinding of SGN peripheral axons during inner ear
640 development. The lack of CHD4 chromatin remodeling activity in SGNs resulted in aberrant axon
641 guidance. The altered pathfinding may affect the transmission of neural signals and innervation of hair
642 cells. These deficits likely contribute to hearing loss in patients with SIHIWES and provide insight into
643 how other neural circuits may be affected.

644

645 CHD4 is a core subunit in the Nucleosome Remodeling and Deacetylase (NuRD) complex (Tong, Hassig
646 et al. 1998, Xue, Wong et al. 1998, Zhang, LeRoy et al. 1998). The NuRD complex acts mainly as a
647 transcriptional repressor and localizes to sites of active transcription. At these sites, CHD4 repositions
648 nucleosomes and subunits of the complex, such as histone deacetylases (HDAC) 1 and 2 deacetylate
649 histones (Morra, Lee et al. 2012, Watson, Mahajan et al. 2012). Although CHD4 has many other paralogs,
650 distinct NuRD complexes with individual CHD paralogs (CHD3, CHD4, and CHD5) have specific
651 molecular functions and do not compensate for the loss of a singular CHD. The remaining paralogous

652 CHDs did not compensate for the cellular effects of ablating CHD4 (Nitarska, Smith et al. 2016). CHD4-
653 containing NuRD complexes in the inner ear may contain distinct protein subunits that alter the epigenetic
654 landscape at cis-regulatory regions. Our results suggest a role for CHD4 in axon guidance during SGN
655 development. Even if paralogs were present in SGNs, they did not fully compensate for the observed
656 axon guidance deficits. We used iMOP-derived neurons as a cellular system to study SGN development.
657 We showed increased CHD4 occupancy at distinct sets of promoters and distal enhancers during
658 neuronal differentiation. We propose that CHD4 exerts epigenetic changes on cis-regulatory elements to
659 attenuate transcription of axon guidance genes until the appropriate developmental time. Without CHD4,
660 the core NuRD complex does not form, and axon guidance genes may show increased transcription
661 without NuRD-dependent nucleosome repositioning and histone deacetylase activities. The exquisite
662 temporal transcriptional control of axon guidance genes is likely required to establish the appropriate
663 fasciculation and innervation patterns.

664 Although CHD4 has domains that interact with modified histones, it lacks a specific DNA-binding domain
665 (Reid, Zhong et al. 2024). Motif analysis was performed to identify potential TF that function with CHD4.
666 We identified TF binding motifs within a single CHD4 binding site at promoters of many axon guidance
667 genes. The clustered motifs in some axon guidance genes, such as *Epha4* and *Epha7,* may facilitate
668 cooperative TF binding. Individual transcription factor binding sites often exhibit relatively weak binding
669 affinities. However, when multiple TFs bind nearby, they can engage in protein-protein interactions or
670 induce DNA conformational changes that collectively strengthen their overall DNA binding affinity. This
671 cooperativity often leads to a synergistic activation or repression of gene expression, where the combined
672 effect of multiple TFs is greater than the sum of each TFs contribution (Wang, Xie et al. 2025). The
673 synergistic binding of TFs with nucleosome remodeling activity from CHD4 may allow for high specificity
674 and tune transcriptional regulation for precise control of axon guidance genes.

675 The various distinct motifs within a cluster also highlight combinatorial control of transcription.
676 Transcription is not typically governed by a single regulatory element but rather by the intricate interplay

677 of multiple TFs. These regulatory modules may serve as integration points for diverse cellular signals,
678 allowing transcription only when a specific combination of TFs is present during development. This
679 combinatorial logic could enable complex regulatory programs to coordinate distinct steps of axon
680 guidance in the cochlea.

681

682 Our identified candidate set of Eph receptors and ephrin ligand genes (*Epha4*, *Epha7*, and *Efnb2*) is
683 noteworthy since it suggests that the combination of axon guidance genes contributes to the wiring of the
684 developing cochlea. Eph receptors are a family of receptor tyrosine kinases that mediate many essential
685 processes through promiscuous interactions with membrane-bound ephrin ligands (Kania and Klein
686 2016). Identifying Eph receptors and their ephrin ligands in the cochlea is particularly challenging. The
687 cochlea's intricate structure makes isolating specific Eph/ephrin interactions complicated without
688 disrupting the function of other cell types in the tissue. The Eph/ephrin system also features significant
689 redundancy and promiscuity, where multiple receptors can bind to the same ligand and vice versa,
690 complicating the identification of specific functional roles. Genetic knockout models often show
691 compensatory mechanisms among *Eph* family members, masking phenotypic effects and making
692 functional studies even more complex. Here, we used the epigenetic modification of regulatory elements
693 around a candidate set of axon guidance genes responsible for assembling neural circuits in the cochlea.
694

695 Ephrins are divided into the glycosyl-phosphatidylinositol (GPI) linked ephrin-A and the transmembrane
696 ephrin-B ligands. Ephrins (EFN) bind to Eph receptors (EPH) of the same class, except for EPHA4.
697 EPHA4 interacts with EFNA, B2, and B3 ligands. Deletion of *Epha4* showed ectopic innervation of outer
698 hair cells by a subset of type I SGNs (Defourny, Poirrier et al. 2013). EPHA4 interacts with EFNA5 to
699 control target specification, expressed primarily in OHCs and a subset of type I SGNs. Previously, *Efna5*
700 was reported to be expressed in a subset of type I SGNs, but recent evidence implicated *Efna5* mainly
701 in type II SGNs (Petitpre, Wu et al. 2018, Sanders and Kelley 2022). The otic mesenchyme surrounding

702 the SGN axons also expresses *EphA4* (Coate, Spita et al. 2015). This pattern of EPHA4 expression
703 guides fasciculation through EFNB2 interactions in the developing SGN axons. Another *Eph* receptor,
704 *EphA7*, in SGNs, is required for neurite outgrowth. Loss of *EphA7* resulted in more sparse fiber bundles
705 and fewer synaptic contacts on inner hair cells (Kim, Ibrahim et al. 2016). *EfnB2* is one of the ephrin
706 ligands, and a high level of *Efnb2* mRNA expression was detected during SGN development, especially
707 at E13.5 and E15.5, when SGN fasciculation initiates. Deletion of *Efnb2* in SGNs showed defective
708 fasciculation of inner radial bundles and an increased number of aberrantly crossing SGN axons between
709 fascicles (Micucci, Sperry et al. 2015). These studies implicate the function of ephrin signaling in
710 developing peripheral auditory circuits.
711
712 Although we observed axon guidance deficits in the *Chd4* cKO cochleae, the phenotypes are distinct.
713 Using the *Ngn1* CreER^{T2}, we only perturbed SGNs while leaving the other cell types, such as hair cells
714 and otic mesenchyme, untouched. Instead of inactivating the function of ephrin receptor or ephrin ligands,
715 *Chd4* deletion increased *Epha4, Epha7, and Efnb2* transcript levels in SGNs, revealing a molecular
716 perturbation relevant to SIHWES disease. The *Chd4* cKO model also differs from the Eph receptor and
717 Ephrin ligand single knockouts because it affects the expression of multiple axon guidance genes. The
718 subtle cellular phenotypes in single *Eph* and *Efn* knockout mice suggest that the proper wiring of the
719 peripheral auditory circuit may require the combined effects of multiple *Eph* and *Efn* members. Finally,
720 the *Chd4* cKO model differs from ablating *Eph* and *Efn* genes because it increases transcription of its
721 target genes. Our findings align with the function of numerous *Eph* and *Efn* genes during SGN
722 development and suggest that CHD4 may coordinate the expression levels of several *Eph* and *Efn* to
723 shape the type I and II SGN innervation patterns.
724
725 Congenital hearing loss syndromes are often associated with pathogenic genetic variants in a single
726 gene. Hearing loss can be syndromic or non-syndromic. Syndromic hearing impairment is associated
727 with clinical features in other organ systems, while non-syndromic hearing impairment has no discernible

728 clinical abnormalities other than in the middle or inner ear. Syndromic hearing loss accounts for over 400
729 genetic syndromic hearing loss conditions (Toriello, Reardon et al. 2004). The characteristics of
730 syndromic hearing loss vary among the different syndromes and affect hearing in either one or both ears.
731 The extent of hearing loss varies dramatically and can range from profound to mild. Different syndromes
732 show distinct features of hearing loss at various sound frequencies. Improper development or dysfunction
733 of the sensory cells and neurons of the inner ear correlates with many forms of syndromic hearing loss.
734 Patients with Sifrim-Hitz-Weiss disease show variable congenital disabilities. This observation is
735 reminiscent of CHARGE syndrome, a genetic disorder caused by pathogenic variants in CHD7. CHD7
736 and CHD4 are part of the chromodomain helicase DNA-binding protein family (Micucci, Sperry et al.
737 2015). Global chromatin regulators such as CHD7 and CHD4 can robustly affect transcription and trigger
738 cell-autonomous changes during critical periods in development. We show that altering the epigenetic
739 landscape by deleting CHD4 early during otic development (E8.5-E10.5) affects pathfinding and
740 connectivity of SGN peripheral axons at multiple steps during axon guidance and may contribute to
741 hearing loss in SIHIWES.

742 Although the phenotype is robust, the penetrance is variable. We believe this is a central aspect observed
743 in mutations of chromodomain helicase DNA-binding proteins. Cellular heterogeneity may contribute to
744 the variable phenotype. There are four distinct subtypes of SGNs: type Ia, Ib, Ic, and type II (Petitpre, Wu
745 et al. 2018, Shrestha, Chia et al. 2018, Sun, Wang et al. 2022). CHD4 may function differently in each
746 neuronal subtype, resulting in differing cellular phenotypes. The difference is evident in the axon guidance
747 phenotypes observed in type I compared to type II neurons. Ablation of CHD4 affected the fasciculation
748 of radial fibers and branching in the inner spiral plexus region for type I SGNs. In contrast, type II neurons
749 displayed a circuitous path to innervate the base of outer hair cells and inappropriate turning at the outer
750 hair cell region. Deleting CHD4 affected the peripheral axons differently in type I and II SGNs.
751

752 In addition to the heterogeneity of neuronal subtypes, variability within type I and II fibers was also
753 observed. The phenotypic variability includes the extent of type I radial fiber bundling and branching of
754 terminals in the inner spiral plexus. CHD4 function in SGN type Ia, b, and c fibers may contribute to the
755 observed variability. Cellular heterogeneity, however, cannot be attributed to the improper turning of
756 some type II peripheral axons. Some type II fibers are seemingly unaffected, whereas others turn in the
757 opposite direction. Stochasticity in molecular processes may be a contributing mechanism. Stochastic
758 gene expression involves biochemical processes such as transcription and translation. The limiting
759 number of molecules that catalyze transcription leads to biological variability, as observed by the dramatic
760 differences in transcript levels even within isogenic cells (Raj and van Oudenaarden 2008). Deletion of
761 CHD4 may alter the chromatin state of cis-regulatory elements and impact the stochasticity in
762 transcription. The epigenetic perturbation could increase both transcript levels and the variance of
763 specific genes after ablating CHD4. We showed an increase in the median number of *Epha4, Epha7,*
764 *and Efnb2* transcripts in *Calb2*-marked SGNs, concomitant with an increase in the variance of the
765 transcript numbers. The increase in transcripts and variance was specific for *Epha4, Epha7, and Efnb2*,
766 not *Calb2*. The larger variance results in a broader distribution of neurons with *Epha4, Epha7, and Efnb2*
767 and displays a cell population that exceeds the normal range of *Epha4, Epha7, and Efnb2* levels in control
768 SGNs. The percentage of neurons with increased *Epha4, Epha7, and Efnb2* transcripts may possess
769 altered protein expression levels of EPHA4, EPHA7, and EFNB2 and perturb axon guidance. In contrast,
770 cells that retain *Epha4, Epha7, and Efnb2* transcripts within the normal range may retain normal axon
771 pathfinding. The increase in transcriptional variance may contribute to the heterogeneous cellular
772 phenotypes observed for type I and type II SGNs.
773
774 In summary, multiple axon guidance deficits of type I and II SGNs were observed using a *Chd4*
775 conditional knockout mouse model. These deficits likely arise at different developmental time points and
776 implicate CHD4 function at varying steps of SGN pathfinding. The candidate CHD4 binding sites include
777 promoters and enhancers that regulate the transcription of a subset of *Eph* receptors and *Efn* ligands.

778 CHD4, as part of the core NuRD complex, may impose a repressive epigenetic state on these cis-
779 regulatory elements to attenuate transcription until the appropriate time during development. Inactivation
780 of CHD4 increases transcript levels of axon guidance genes to perturb the stereotypic peripheral axon
781 patterning. These results also have a broader implication on the formation of neuronal circuits during
782 development and regeneration.

783 **Conflict of Interest:**

784 The authors declared no potential conflicts of interest in the research, authorship, and publication of this
785 article.

786

787 **Accession Numbers:**

788 The GEO accession number for the CUT&Tag raw fastq data, along with the processed bigwig and
789 SEACR peak files, is GSE250033. IGV session with the CUT&Tag tracks can be provided upon request.

790

791 **Author contribution:**

792 JK and EM were responsible for the experimental design, execution of experiments, and the acquisition
793 and analysis of immunofluorescent images. JN performed CUT&Tag, and JQ analyzed data from
794 CUT&Tag. KYK assisted in CUT&Tag and RNAscope analysis. KYK conceived the project and performed
795 motif analysis. JK, EM, and KYK wrote the manuscript.

796

797 **Acknowledgments:**

798 We thank Dr. Katia Georgopoulos (Mass General Hospital) and Dr. Lisa Goodrich (Harvard Medical
799 School) for providing the *Chd4*$^{flox/flox}$ animals and advice on dosing the Ngn1 CreER^{T2} animals,
800 respectively. We acknowledge Dr. Alejandra Laureano and Ms. Anna Maria Hinman for initially
801 generating and maintaining the mouse line. NIH R01 DC015000 supported this work for KYK.

Fig. 1

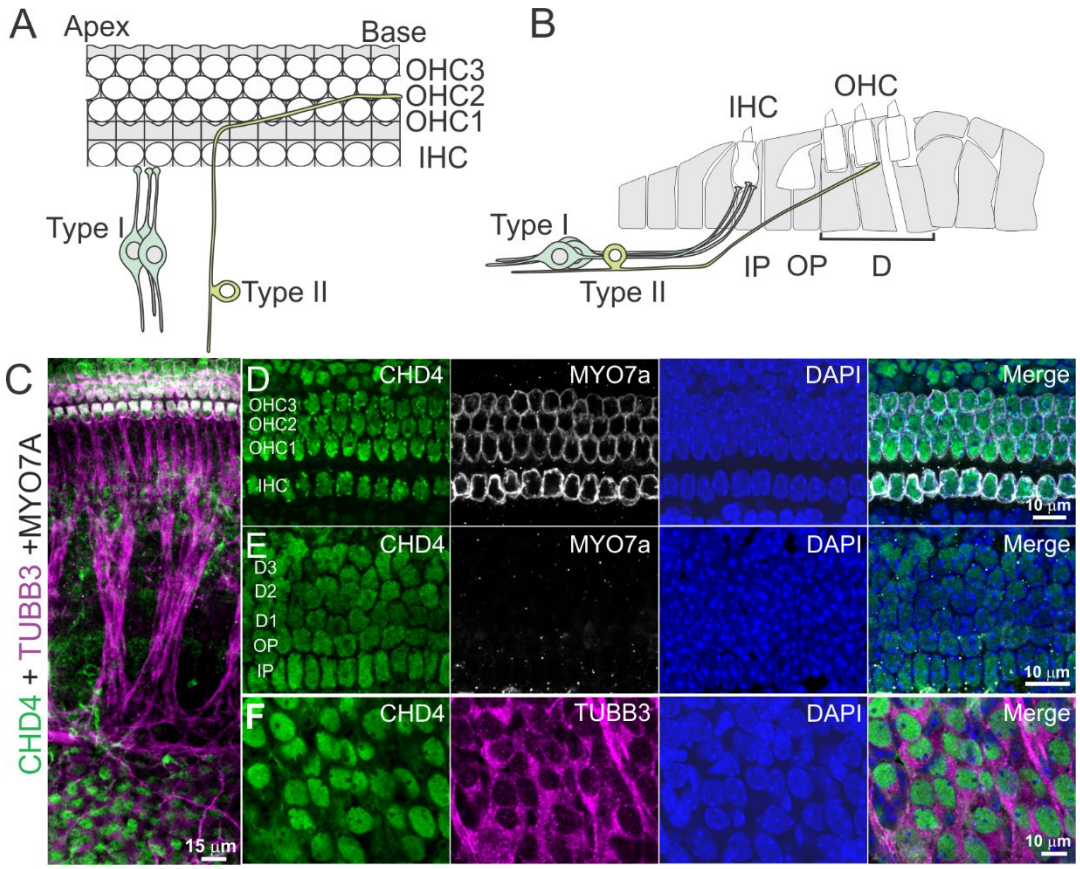
A
Apex
Base
OHC3
OHC2
OHC1
IHC
Type I
Type II
B
IHC
OHC
Type I
Type II
IP
OP
D
C
CHD4 + TUBB3 +MYO7A
15 µm
D
CHD4
MYO7a
DAPI
Merge
OHC3
OHC2
OHC1
IHC
10 µm
E
CHD4
MYO7a
DAPI
Merge
D3
D2
D1
OP
IP
10 µm
F
CHD4
TUBB3
DAPI
Merge
10 µm

Fig. 2

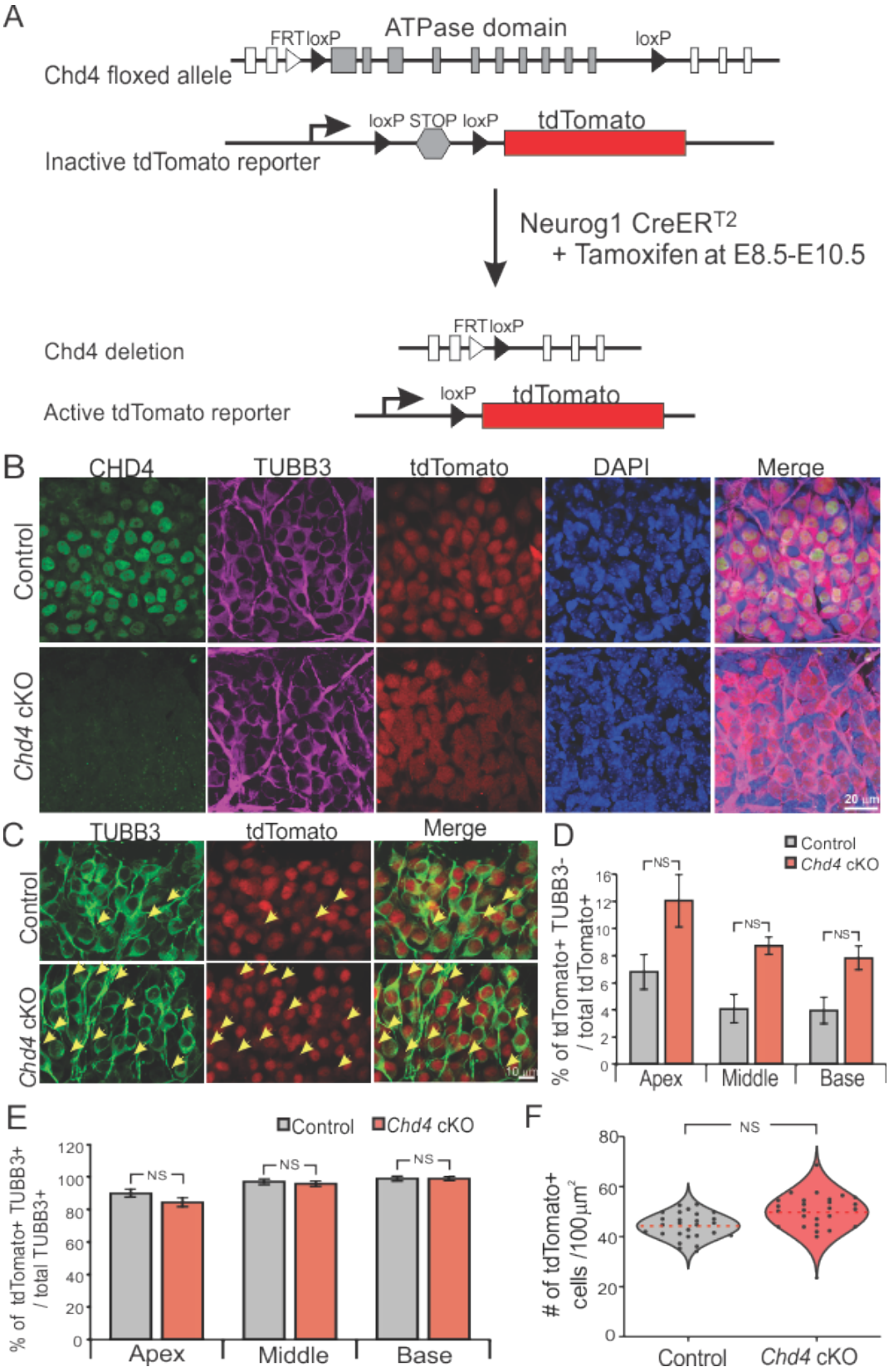
A
Chd4 floxed allele
FRT loxP
ATPase domain
loxP
Inactive tdTomato reporter
loxP STOP loxP
tdTomato
Neurog1 CreERT2
+ Tamoxifen at E8.5-E10.5
Chd4 deletion
FRT loxP
Active tdTomato reporter
loxP
tdTomato
B
CHD4
TUBB3
tdTomato
DAPI
Merge
Control
Chd4 cKO
20 µm
C
TUBB3
tdTomato
Merge
Control
Chd4 cKO
10 µm
D
Control
Chd4 cKO
% of tdTomato+ TUBB3- / total tdTomato+
NS
Apex
Middle
Base
E
Control
Chd4 cKO
% of tdTomato+ TUBB3+ / total TUBB3+
NS
Apex
Middle
Base
F
NS
# of tdTomato+ cells /100µm²
Control
Chd4 cKO

Fig. 3

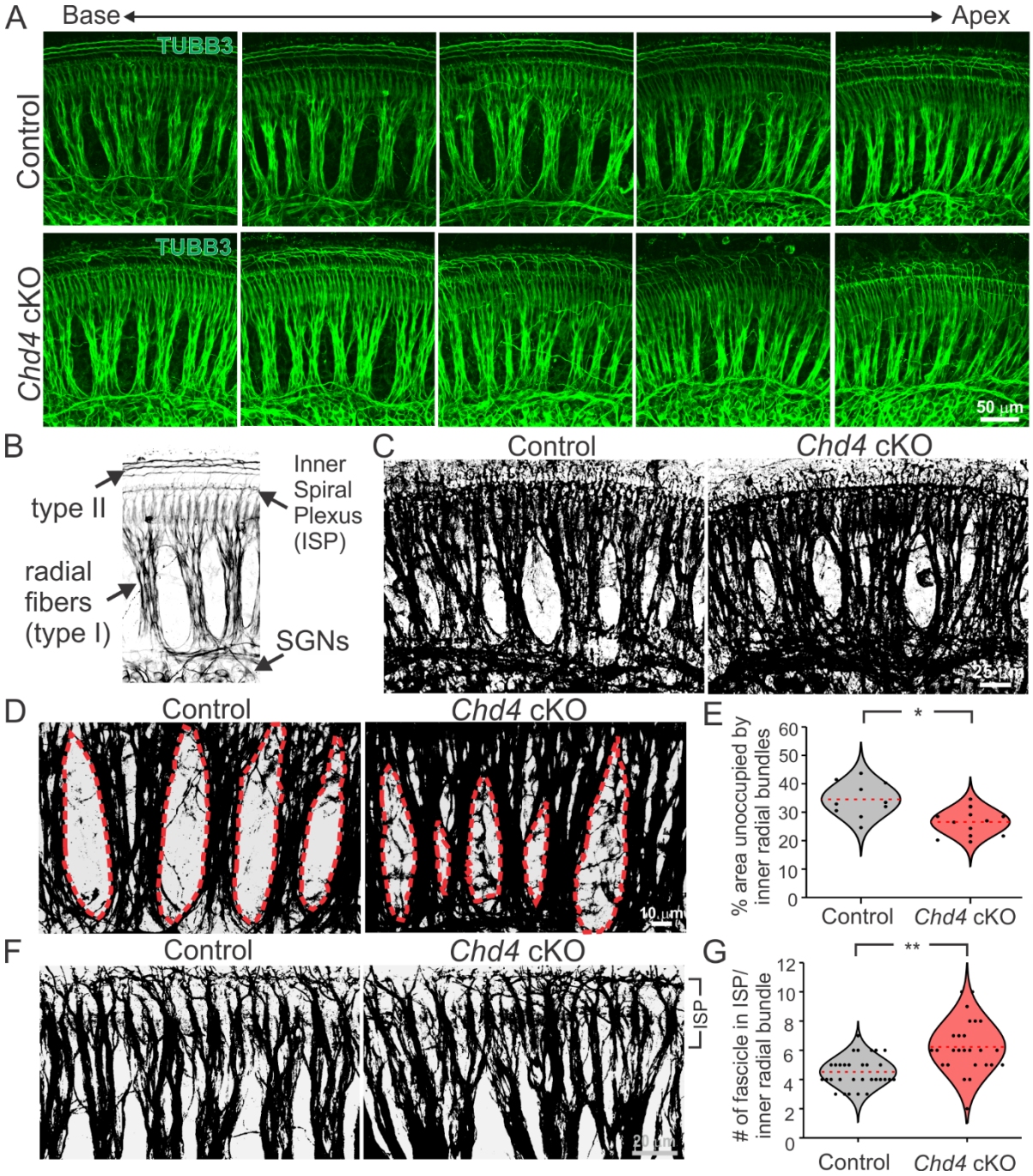
A
Base
Apex
TUBB3
Control
TUBB3
Chd4 cKO
50 µm
B
type II
Inner Spiral Plexus (ISP)
radial fibers (type I)
SGNs
C
Control
Chd4 cKO
D
Control
Chd4 cKO
10 µm
E
% area unoccupied by inner radial bundles
60
50
40
30
20
10
0
*
Control
Chd4 cKO
F
Control
Chd4 cKO
ISP
G
# of fascicle in ISP/ inner radial bundle
12
10
8
6
4
2
0
**
Control
Chd4 cKO

Fig. 4

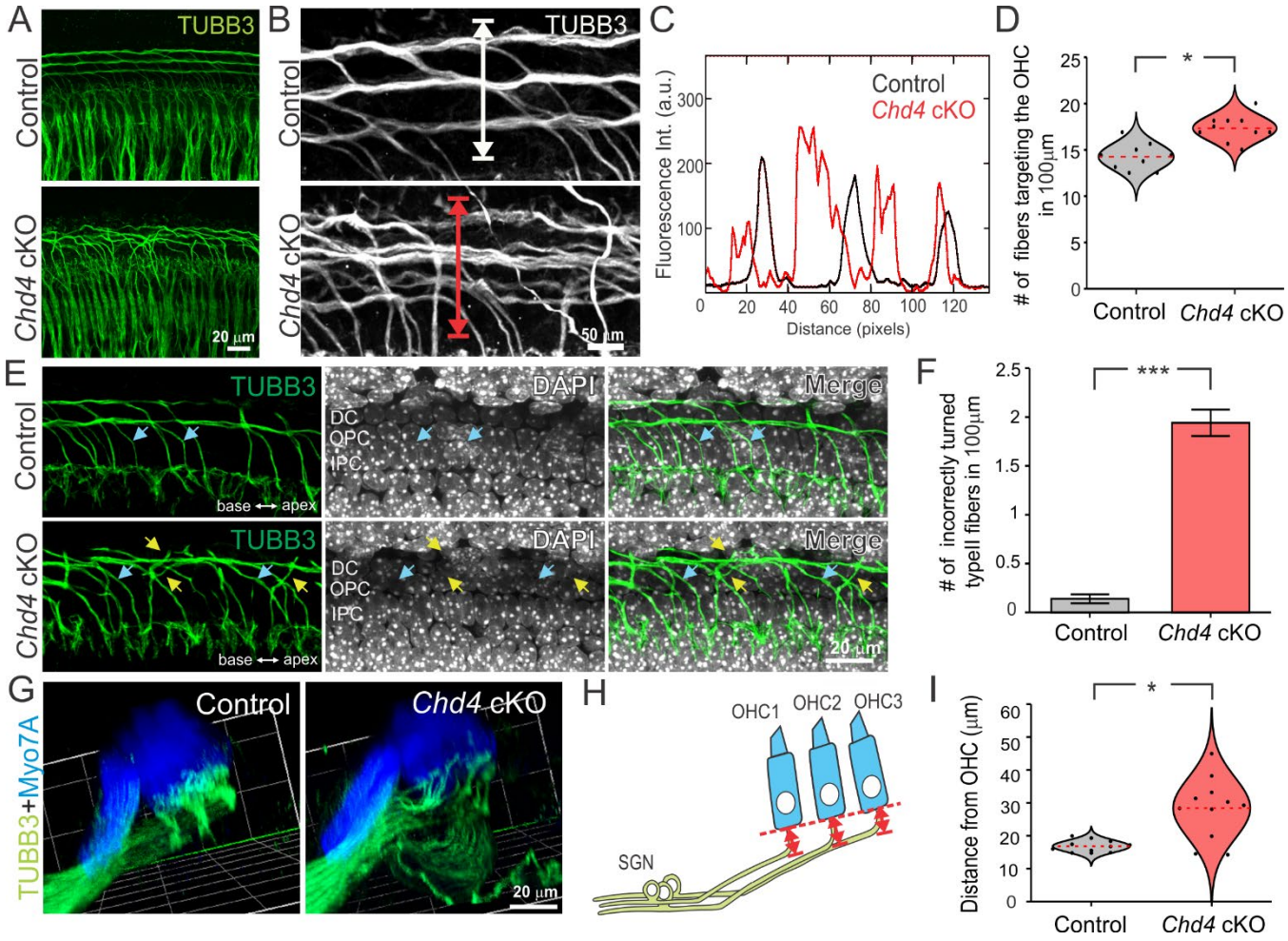
A
TUBB3
Control
Chd4 cKO
20 µm
B
TUBB3
Control
Chd4 cKO
50 µm
C
Control
Chd4 cKO
Fluorescence Int. (a.u.)
Distance (pixels)
D
# of fibers targeting the OHC in 100µm
Control
Chd4 cKO
E
TUBB3
DAPI
Merge
DC
OPC
IPC
base ↔ apex
20 µm
F
# of incorrectly turned typell fibers in 100µm
Control
Chd4 cKO
G
Control
Chd4 cKO
TUBB3+Myo7A
20 µm
H
OHC1
OHC2
OHC3
SGN
I
Distance from OHC (µm)
Control
Chd4 cKO

Fig. 5

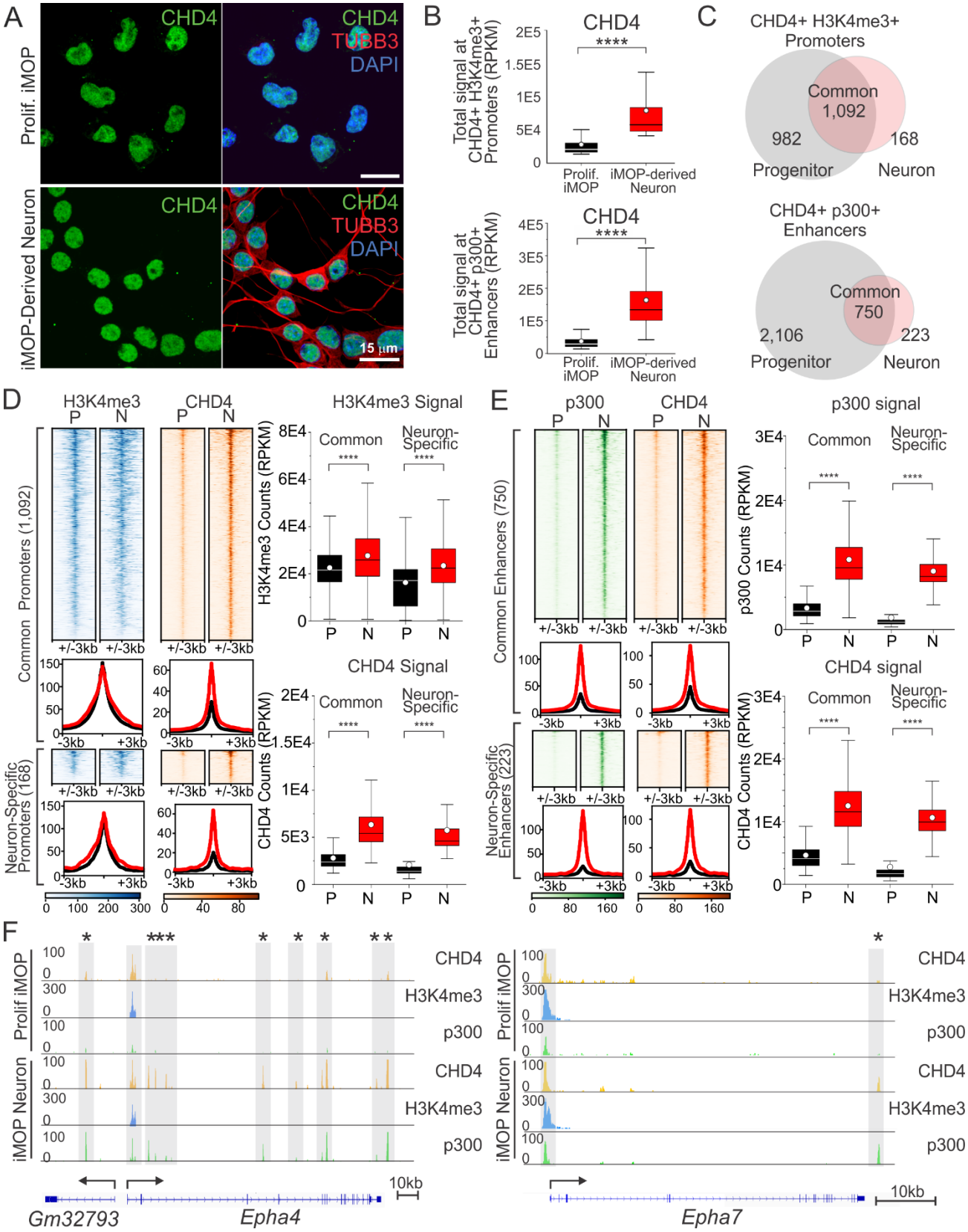
A
Prolif. iMOP
iMOP-Derived Neuron
CHD4
CHD4
TUBB3
DAPI
15 µm
B
CHD4
Total signal at CHD4+ H3K4me3+ Promoters (RPKM)
Prolif. iMOP
iMOP-derived Neuron
Total signal at CHD4+ p300+ Enhancers (RPKM)
C
CHD4+ H3K4me3+ Promoters
Common 1,092
982 Progenitor
168 Neuron
CHD4+ p300+ Enhancers
Common 750
2,106 Progenitor
223 Neuron
D
H3K4me3
CHD4
H3K4me3 Signal
CHD4 Signal
Common Promoters (1,092)
Neuron-Specific Promoters (168)
H3K4me3 Counts (RPKM)
CHD4 Counts (RPKM)
Common
Neuron-Specific
E
p300
CHD4
p300 signal
CHD4 signal
Common Enhancers (750)
Neuron-Specific Enhancers (223)
p300 Counts (RPKM)
F
Prolif iMOP
iMOP Neuron
CHD4
H3K4me3
p300
Gm32793
Epha4
Epha7
10kb

Fig. 6

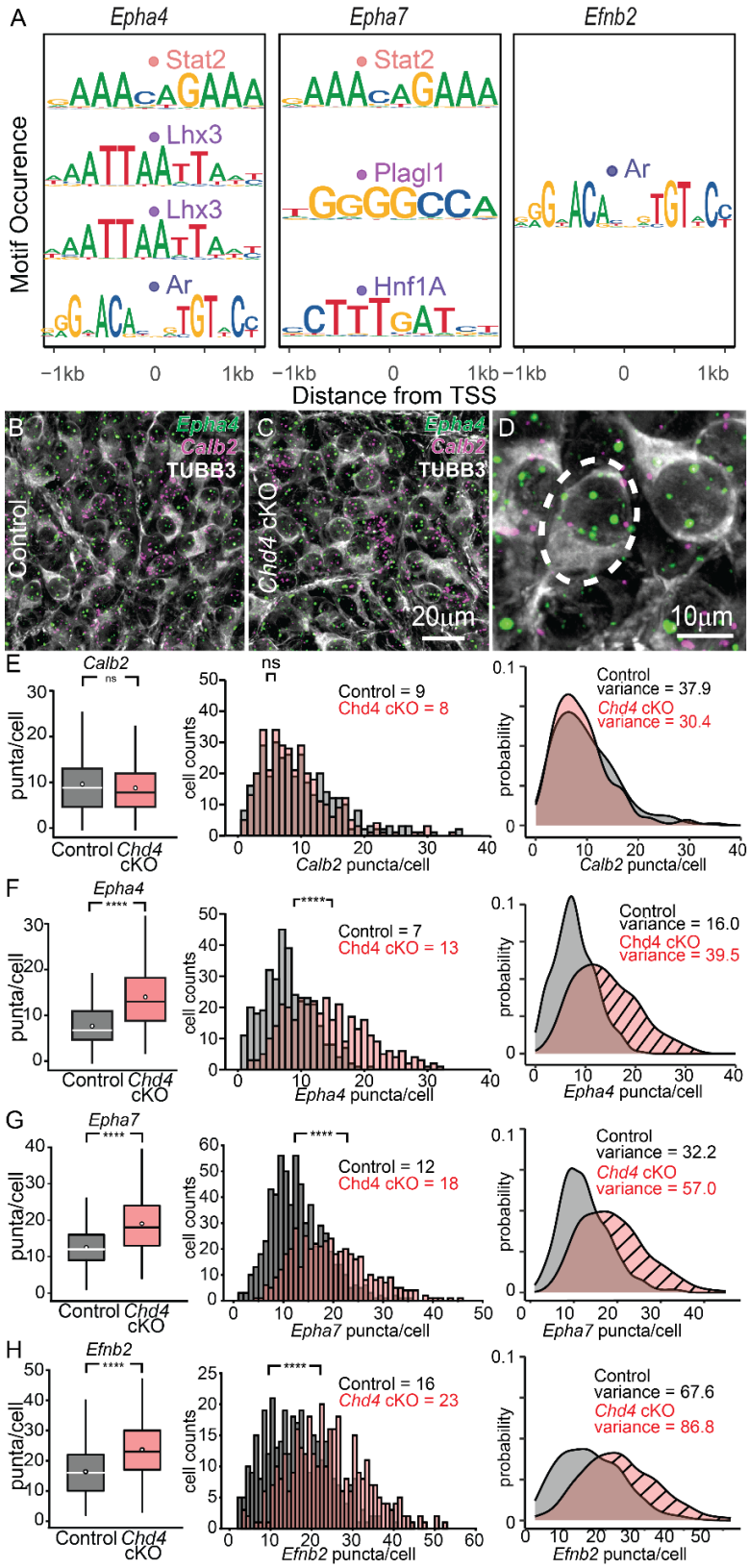
A
Epha4
Epha7
Efnb2
Motif Occurence
Stat2
Lhx3
Lhx3
Ar
Stat2
Plagl1
Hnf1A
Ar
−1kb
0
1kb
Distance from TSS
B
C
D
Epha4
Calb2
TUBB3
Control
Chd4 cKO
20μm
10μm
E
Calb2
ns
punta/cell
Control
Chd4 cKO
cell counts
Control = 9
Chd4 cKO = 8
Calb2 puncta/cell
probability
Control
variance = 37.9
Chd4 cKO
variance = 30.4
F
Epha4
****
Control = 7
Chd4 cKO = 13
Epha4 puncta/cell
Control
variance = 16.0
Chd4 cKO
variance = 39.5
G
Epha7
Control = 12
Chd4 cKO = 18
Epha7 puncta/cell
Control
variance = 32.2
Chd4 cKO
variance = 57.0
H
Efnb2
Control = 16
Chd4 cKO = 23
Efnb2 puncta/cell
Control
variance = 67.6
Chd4 cKO
variance = 86.8

802 **Figure Legend**

803

804 **Figure 1. CHD4 expression in the spiral ganglion and the organ of Corti.**

805 (A) Top-down schematic depicting the innervation pattern of type I and II SGNs. Type I SGNs extend
806 single, unbranched neurites that innervate an individual inner hair cell (IHC). Type II SGNs extend
807 neurites into the outer hair cell (OHC) region, turn basally, and can contact multiple OHCs. (B) Sagittal
808 schematic of the innervation pattern. Multiple Type I SGNs innervate a single IHC. Type II neurites make
809 a basal turn in the region near Deiters' cells, a supporting cell type. (C) Immunofluorescence labeling of
810 CHD4 (green), TUBB3 (magenta), and MYO7A (white) from a flat-mounted cochlea. TUBB3 and MYO7A
811 label neurons and hair cells, while DAPI (blue) marks nuclei. Different regions of immunolabeled E18.5
812 cochlea. (D) Expression of CHD4 in the single row of inner hair cells (IHC) and the three rows of outer
813 hair cells (OHC1-3). (E) CHD4 labeling in supporting cells, including inner pillar (IP), outer pillar (OP),
814 and three rows of Dieter cells (DC1-3). The nuclei of supporting cells reside underneath hair cells. (F)
815 CHD4 labeling in spiral ganglion neurons. Scale bar as marked.

816

817 **Figure 2. Deletion of *Chd4* from SGNs using Neurog1 CreER^{T2} Chd4 $^{flox/flox}$ mice.**

818 (A) Schematic illustration of Cre-mediated *Chd4* deletion following tamoxifen induction in *Chd4*
819 conditional knockout (cKO) mice containing Neurog1 CreER^{T2}; *Chd4*$^{flox/flox}$; tdTomato alleles.
820 Administration of tamoxifen at E8.5-E10.5 deletes loxP flanked exons coding for the *Chd4* ATPase
821 domain and activates expression of the tdTomato reporter. Animals without the *Chd4* cKO allele
822 (Neurog1 CreER^{T2}; tdTomato) were used as controls. (B) Immunostaining of CHD4 and TUBB3 marked
823 neurons in E18.5 cochlea. tdTomato expression correlates with the presence of Cre activity. Nuclear
824 CHD4 expression was observed in DAPI-marked nuclei in control SGNs but was absent in *Chd4* cKO
825 SGNs after tamoxifen administration. (C) Confocal micrographs from the spiral ganglion. Yellow arrows
826 indicate tdTomato^{+} and TUBB3^{-} cells. (D) Percentages of tdTomato^{+} and TUBB3^{-} cells found within the
827 apex, middle, and base regions of the cochlea (apex, $p < 0.136$, middle, $p < 0.095$; base, $p < 0.148$;

828 control, n=3 and Chd4 cKO, n=3 cochlea) (E) Percentages of cells expressing tdTomato and TUBB3
829 from the base to apex of the cochlea from control and *Chd4* cKO cochleae (apex $p<0.30$; middle $p<0.60$;
830 base, $p < 0.90$; control, n=3 and Chd4 cKO, n=3 cochleae) (F) Normalized number of tdTomato$^+$ cells
831 per 100 μm^2 area in control and Chd4 cKO cochleae ($p < 0.08$; control, n=27 and *Chd4* cKO n=27 images
832 were analyzed from control, n=3 and *Chd4* cKO, n=3 cochleae). The Student's t-test was used for
833 statistical analysis using the number of cochleae. Scale bar as marked.
834
835 **Figure 3. Inner radial bundles display fasciculation defects in *Chd4* cKO cochleae**
836 (A) TUBB3-labeled cochleae from E18.5 control and *Chd4* cKO animals. Images are ordered from base
837 to apex. (B) Depiction of the inner spiral plexus (ISP) near the base of inner hair cells and peripheral
838 projections from type I (radial fibers) and II SGNs from E18.5 cochlea. (C) Binarized images of TUBB3-
839 labeled control and *Chd4* cKO cochleae at E18.5. (D) Regions between radial fiber bundles were outlined
840 in red. (E) The identified areas were quantified and compared between control and *Chd4* cKO ($p < 0.05$;
841 control, n=10 and *Chd4* cKO, n=13 images were analyzed from control, n=3 and *Chd4* cKO, n=3
842 cochleae). (F) Binarized images of control and *Chd4* cKO E18.5 cochleae around the ISP. (G)
843 Comparison of the normalized number of fascicles in the ISP per radial bundle between control and *Chd4*
844 cKO cochleae ($p < 0.01$; control, n=31 and *Chd4* cKO, n=26 bundles were analyzed from control, n=5
845 and *Chd4* cKO, n=3 cochleae). The Student's t-test was used for statistical analysis. Scale bars as
846 marked.
847
848 **Figure 4. Type II spiral ganglion neurons display turning defects in the *Chd4* cKO mice.**
849 (A) TUBB3-labeled neuronal projections in E18.5 control and *Chd4* cKO cochleae**.** Type II fibers can be
850 distinguished by their anatomical location. (B) Type II fibers from the control show stereotypic tracks that
851 turn towards the base and travel along individual rows of outer hair cells. *Chd4* cKO type II fibers showed
852 aberrant fiber tracks. (C) The intensity profile plot was measured along the white and red lines to highlight
853 the differences between the control and Chd4 cKO fiber tracks. Peaks from fluorescence intensity

854 measurements indicate the presence of a fiber track. Control cochleae show three peaks correlating with
855 fibers along the three rows of outer hair cells. Chd4 cKO samples showed an additional peak, suggesting
856 aberrant fiber tracks. (D) Normalized number of fibers entering the OHC region per 100 μm from control
857 and *Chd4* cKO E18.5 cochleae ($p < 0.03$; control, n=9 and *Chd4* cKO, n=10 images were analyzed from
858 control, n=3 and *Chd4* cKO, n=3 cochleae). (E) Optical section from TUBB3 and DAPI-labeled confocal
859 micrographs that visualize fibers entering the OHC region. Blue arrows mark correctly turned while yellow
860 arrows show incorrect turning type II fibers. (F) The normalized number of incorrectly turned type II fibers
861 per 100 μm from control and *Chd4* cKO E18.5 cochleae ($p < 2.82 \times 10^{-4}$; control, n=3 and *Chd4* cKO,
862 n=3 cochleae). (G) 3D-rendered images highlighting the axonal trajectory from SGNs (TUBB3+, green)
863 to hair cells (MYO7A+, blue). (H) Schematic of peripheral SGN axonal projections to outer hair cells. Red
864 arrows represent the distance between contact points in the OHCs (red dashed line) and the final turning
865 point on the incoming axon. (I) Average distances from the base of outer hair cells to the axon bundles
866 showed differences between control and *Chd4* cKO ($p < 0.03$; control, n=11, and *Chd4* cKO, n=11 images
867 were analyzed from control, n=3 and *Chd4* cKO, n=3 cochleae). The Student's t-test was used for
868 statistical analysis. Scale bars as marked.
869
870 **Figure 5. CHD4 binds to the promoters of genes involved in axon guidance, including members**
871 **of the ephrin family of signaling molecules, in iMOP-derived neurons.**
872 (A) Overlap of CHD4 in the nuclei (DAPI) of proliferating iMOP and TUBB3-labeled iMOP-derived
873 neurons. CUT&Tag was performed using proliferating iMOP cells and iMOP-derived neurons. CUT&Tag
874 peaks were identified using SEACR. (B) Box and whisker plots show SEACR total signals for CHD4 at
875 CHD4+ H3K4me3+ and CHD4+p300+ in proliferating iMOPs were significantly different from that in
876 iMOP-derived neurons ($p < 2.20 \times 10^{-16}$). (C) Venn diagrams show the overlap of CHD4+ H3K4me3+
877 promoters and CHD4+ p300+ enhancers between progenitors (P) and neurons (N). (D) Heatmaps and
878 profile plots show H3K4me3 and CHD4 signals within +/- 3kb of the summit regions of common and
879 neuron-specific promoters. Box and whisker plots show significantly increased H3K4me3 and CHD4

880 signals at both common and neuron-specific promoters in progenitors compared to neurons. (E)
881 Heatmaps and profile plots show p300 and CHD4 signals within +/- 3kb of the summit regions of common
882 and neuron-specific enhancers. Box and whisker plots show significantly increased p300 and CHD4
883 signals at both common and neuron-specific enhancers in progenitors compared to those in neurons. (F)
884 Enrichment of CHD4 (orange), H3K4me3 (blue), and p300 (green) at the specified genomic region of
885 *Epha4* and *Epha7* in proliferating iMOPs and iMOP-derived neurons. Highlighted genomic regions
886 represent H3K4me3-marked promoters. Highlighted regions with asterisks denote the regions with
887 increased enrichment of CHD4 and p300 in iMOP-derived neurons. The number of asterisks denotes the
888 peaks with increased CHD4 and p300 levels. The Wilcoxon rank-sum test was used for statistical
889 analysis. Scale bars as marked.
890
891 **Figure 6. *Chd4* cKO shows an increased *Eph and Efn* mRNA expression in SGNs.**
892 (A) Occurrence and position of transcription factor (TF) binding motifs relative to the transcriptional start
893 site (TSS) at *Epha4*, *Epha7,* and *Efnb2*. E16.5 (B) control and (C) *Chd4* cKO cochlea were processed
894 for single-molecule RNA fluorescence *in situ* hybridization (smFISH) with probes against *Epha4* and
895 *Calb2.* Cochleae were immunolabeled with TUBB3 to visualize SGNs. (D) The number of puncta for
896 individual TUBB3-labeled cells (dashed line) was quantified. (E) Box plots representing median (lines)
897 and mean (circles) values after comparing smFISH puncta between control and *Chd4* cKO samples for
898 *Calb2* and distribution plots of puncta in control and *Chd4* cKO SGNs ($p < 0.13$). Kernel densities for
899 *Calb2* transcripts ($p < 0.04$; control, n=350 cells from 3 cochleae and Chd4 cKO, n=345 cells from 3
900 cochleae). (F) Box and distribution plots of the number of puncta for *Epha4* in control and *Chd4* cKO
901 SGNs ($p < 1.74 \times 10^{-39}$). Kernel density plots for *Epha4* transcripts display the non-overlapping region
902 (hashed region), suggesting an increased probability of cells from *Chd4* cKO with higher levels of *Epha4*
903 transcripts compared to the control ($p < 2.27 \times 10^{-14}$; control, n=350 cells from 3 cochleae and Chd4
904 cKO, n=345 cells from 3 cochleae). (G) Box and distribution plots of *Epha7* transcripts in control and
905 *Chd4* cKO SGNs ($p < 2.48 \times 10^{-45}$). Non-overlapping region of densities in *Epha7* (hashed region)

906 between control and *Chd4* cKO displays an increased probability of cells from *Chd4* cKO with higher
907 levels of *Epha7* ($p < 8.29 \times 10^{-11}$; control, n=632 cells from 4 cochleae and *Chd4* cKO, n=436 cells from
908 3 cochleae). (H) Box and distribution plots of the number of *Efnb2* transcripts in SGNs from control and
909 chd4 cKO ($p < 7.33 \times 10^{-24}$). Kernel density plots for *Efnb2* transcripts show an increased non-overlapping
910 density region of *Efnb2* transcripts from *Chd4* cKO (hashed region) compared to the control. ($p < 0.04$;
911 control, n=363 from 3 cochleae and *Chd4* cKO n=340 cells from 3 cochleae). The Wilcoxon rank-sum
912 test and Levene's test were used for statistical analysis.

Fig. S1

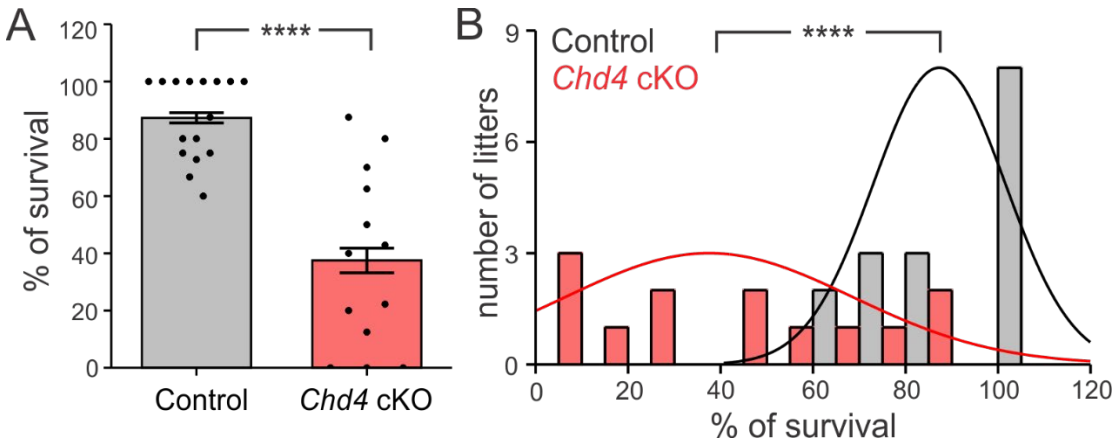
A
120
100
80
60
40
20
0
% of survival
****
Control
Chd4 cKO
B
9
6
3
0
number of litters
Control
Chd4 cKO
****
0
20
40
60
80
100
120
% of survival

Fig. S2

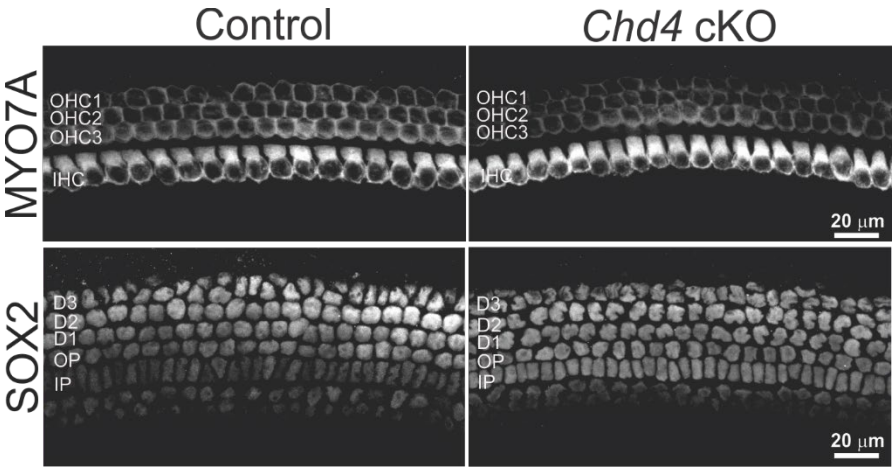
Control
Chd4 cKO
MYO7A
OHC1
OHC2
OHC3
IHC
OHC1
OHC2
OHC3
IHC
20 μm
SOX2
D3
D2
D1
OP
IP
D3
D2
D1
OP
IP
20 μm

Fig. S3

A

ID	Description	p value
0048013	ephrin receptor signaling pathway	4.9E-05
0007411	axon guidance	2.0E-13
1902287	semaphorin-plexin signaling pathway involved in axon guidance	2.7E-02
0007409	axonogenesis	1.6E-14
0006325	chromatin organization	5.1E-14
0007413	axonal fasciculation	1.6E-02

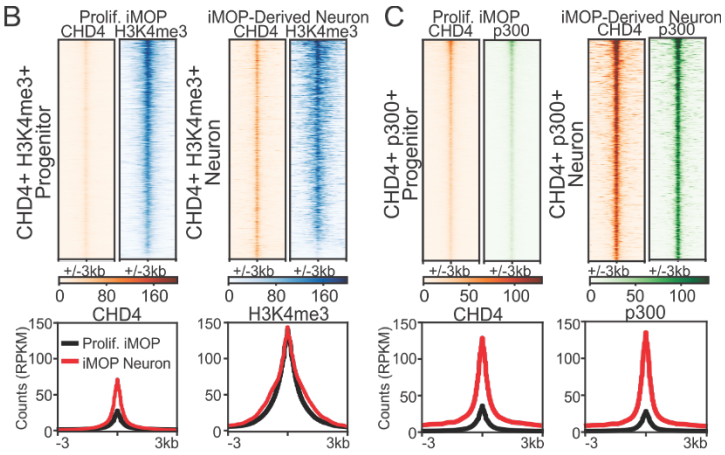

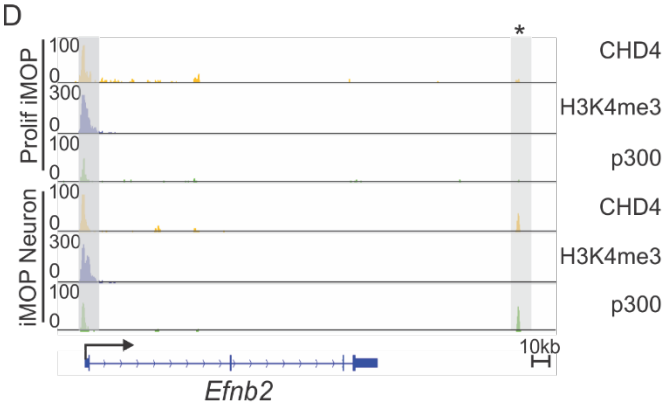

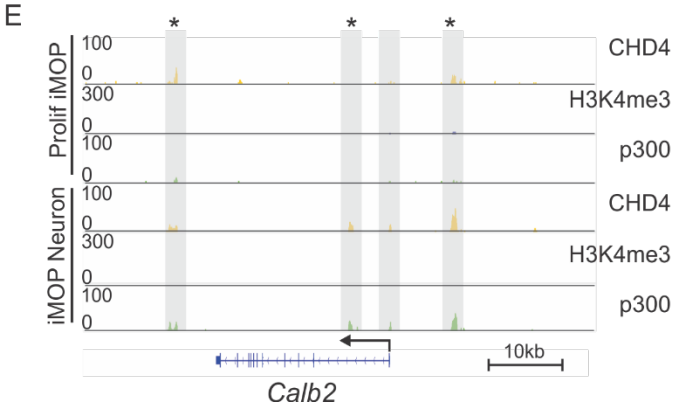

Fig. S4

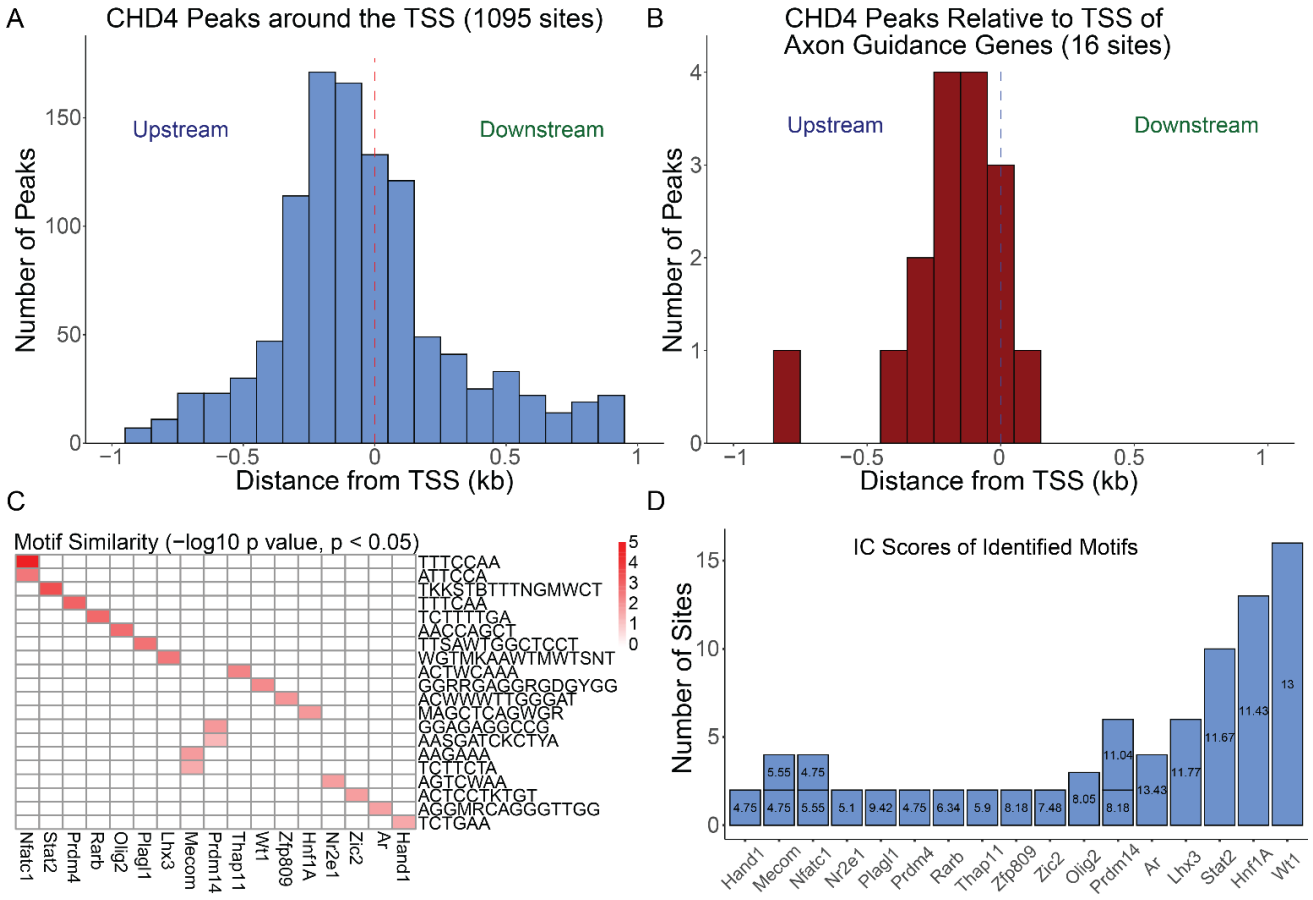
A
CHD4 Peaks around the TSS (1095 sites)
Upstream
Downstream
Number of Peaks
Distance from TSS (kb)
B
CHD4 Peaks Relative to TSS of Axon Guidance Genes (16 sites)
Upstream
Downstream
Number of Peaks
Distance from TSS (kb)
C
Motif Similarity (−log10 p value, p < 0.05)
TTTCCAA
ATTCCA
TKKSTBTTTNGMWCT
TTTCAA
TCTTTTGA
AACCAGCT
TTSAWTGGCTCCT
WGTMKAAWTMWTSNT
ACTWCAAA
GGRRGAGGRGDGYGG
ACWWWTTGGGAT
MAGCTCAGWGR
GGAGAGGCCG
AASGATCKCTYA
AAGAAA
TCTTCTA
AGTCWAA
ACTCCTKTGT
AGGMRCAGGGTTGG
TCTGAA
Nfatc1
Stat2
Prdm4
Rarb
Olig2
Plagl1
Lhx3
Mecom
Prdm14
Thap11
Wt1
Zfp809
Hnf1A
Nr2e1
Zic2
Ar
Hand1
D
IC Scores of Identified Motifs
Number of Sites
Hand1
Mecom
Nfatc1
Nr2e1
Plagl1
Prdm4
Rarb
Thap11
Zfp809
Zic2
Olig2
Prdm14
Ar
Lhx3
Stat2
Hnf1A
Wt1

913

Fig. S5

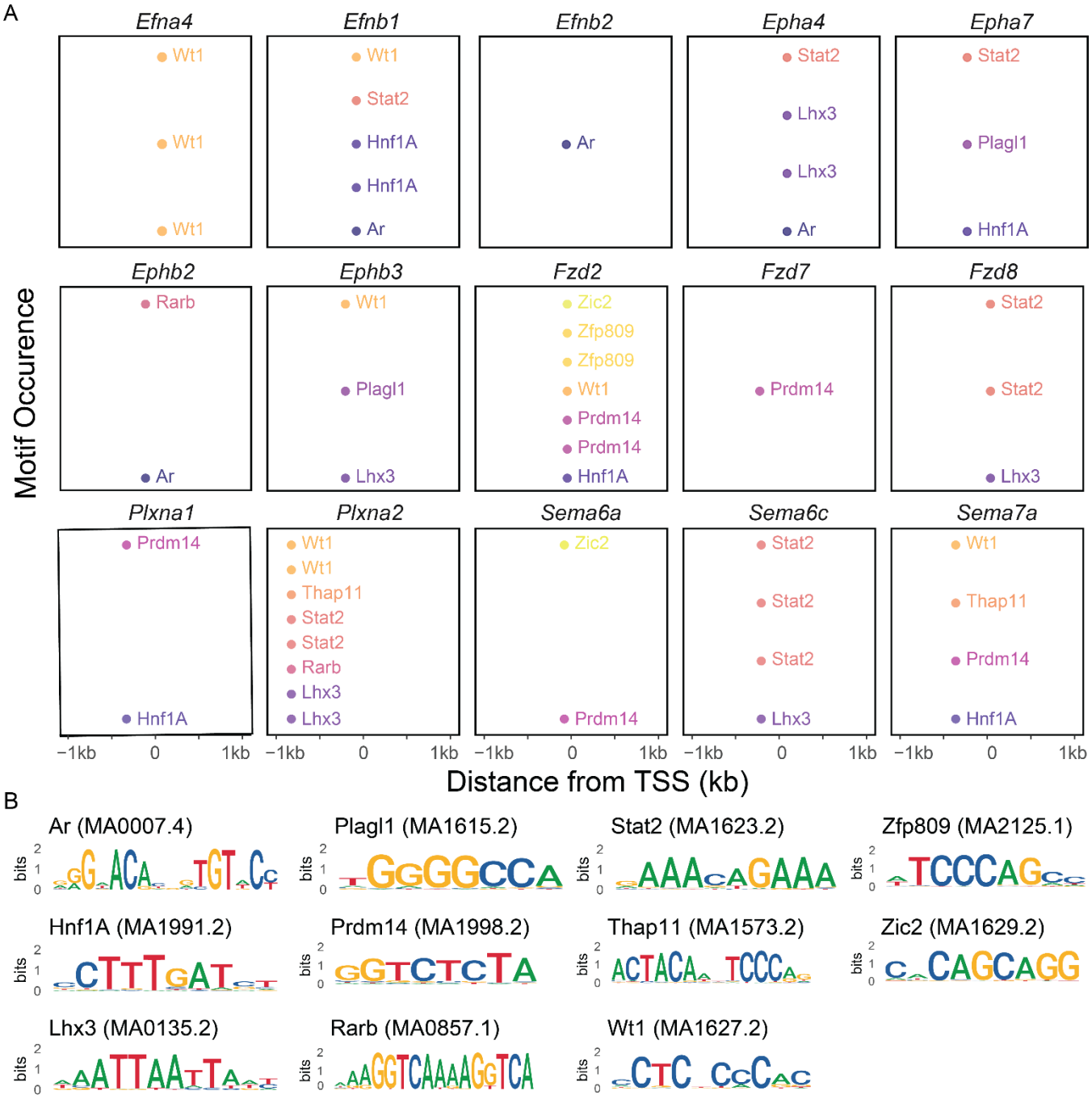
A
Efna4
Wt1
Wt1
Wt1
Efnb1
Wt1
Stat2
Hnf1A
Hnf1A
Ar
Efnb2
Ar
Epha4
Stat2
Lhx3
Lhx3
Ar
Epha7
Stat2
Plagl1
Hnf1A
Ephb2
Rarb
Ar
Ephb3
Wt1
Plagl1
Lhx3
Fzd2
Zic2
Zfp809
Zfp809
Wt1
Prdm14
Prdm14
Hnf1A
Fzd7
Prdm14
Fzd8
Stat2
Stat2
Lhx3
Plxna1
Prdm14
Hnf1A
Plxna2
Wt1
Wt1
Thap11
Stat2
Stat2
Rarb
Lhx3
Lhx3
Sema6a
Zic2
Prdm14
Sema6c
Stat2
Stat2
Stat2
Lhx3
Sema7a
Wt1
Thap11
Prdm14
Hnf1A
Motif Occurence
−1kb
0
1kb
Distance from TSS (kb)
B
Ar (MA0007.4)
Plagl1 (MA1615.2)
Stat2 (MA1623.2)
Zfp809 (MA2125.1)
Hnf1A (MA1991.2)
Prdm14 (MA1998.2)
Thap11 (MA1573.2)
Zic2 (MA1629.2)
Lhx3 (MA0135.2)
Rarb (MA0857.1)
Wt1 (MA1627.2)
bits

914 **Supplemental Figure Legend**

915

916 **Supplemental Figure 1. Survival of *Chd4* conditional knockout mice**

917 (A) Average percentage of viable pups from all collected control and mutant litters ($p < 4.36 \times 10^{-6}$; control,
918 n=16 and *Chd4* cKO, n=13 litters). (B) Distribution of the percentages of surviving E18.5 pups from control
919 and *Chd4* cKO litters after tamoxifen treatment. The p-value and sample size are listed. The Student's t-
920 test was used for statistical analysis.

921

922 **Supplemental Figure 2. The arrangement of supporting and hair cells is unaffected following the**
923 **deletion of *Chd4* within spiral ganglion neurons**

924 Immunofluorescent labeling of MYO7A and SOX2 marked hair cells and supporting cells from E18.5
925 cochleae. Confocal stacks from control and *Chd4* cKO cochleae with MYO7A-marked hair cells and
926 SOX2-marked supporting cells. OHC (outer hair cell), IHC (inner hair cell), D (Deiters' cells), OP (outer
927 phalangeal cells) and IP (inner phalangeal cells). Scale bar as marked.

928

929 **Supplemental Figure 3. Identifying CHD4 binding at promoters and enhancers of target genes**

930 (A) Table showing Gene Ontology ID, description of each category, and corresponding adjusted p values
931 using the Benjamini-Hochberg method for multiple testing correction. (B) Heatmaps and profile plots of
932 CHD4 and H3K4me3 signals within +/- 3kb of the summit regions of CHD4+ H3K4me3+ in both
933 proliferating iMOP and iMOP-derived neurons. (C) Heatmaps and profile plots of CHD4 and p300 signals
934 within +/- 3kb of the summit regions of CHD4+ p300+ in proliferating iMOPs and iMOP-derived neurons.
935 (D) Enrichment of CHD4 (orange), H3K4me3 (blue), and p300 (green) at the specified genomic regions of
936 *Efnb2* in proliferating iMOPs and iMOP-derived neurons. Highlighted genomic regions represented
937 H3K4me3-marked promoters, while highlighted regions with asterisks denote regions with increased

938 CHD4 and p300 in iMOP-derived neurons. The number of asterisks indicates the number of peaks that
939 show increased CHD4 and p300 levels. Scale bars as marked.
940
941 **Supplemental Figure 4. *De novo* motif discovery and annotation**
942 **(**A) A histogram displaying 1,095 CHD4 peaks relative to the transcriptional start sites (TSS) from all the
943 CHD4 binding sites. The dashed red line separates the upstream and downstream regions at the TSS.
944 (B) Distribution of 16 CHD4 peaks relative to TSS at axon guidance genes. (C) A heatmap depicting the
945 pairwise comparison between a set of *de novo* motif sequences with known transcription factor (TF)
946 names. The consensus sequences are shown on the right, and sites corresponding to binding site of the
947 TFs on the bottom. The color intensity represents the statistical significance similarity comparisons ($p <$
948 0.05). (D) Information Content (IC) scores of annotated motifs showing the number of occurences with
949 the associated Information Content (IC) score. The IC score reflects the specificity or conservation of the
950 motif.
951
952 **Supplemental Figure 5. Motif consensus sequences and occurence**
953 (A) The occurrence and position relative to the TSS of annotated motifs. Each panel represents the
954 genomic region around the TSS of the axon guidance gene. Within each panel, dots represent the
955 occurrence of a TF motif relative to the TSS. (B) Sequence logos for the various TF binding motifs
956 identified in the axon guidance genes. Each logo contains the motif name and its unique JASPAR
957 accession number.
958

Table 1. List of primers used for genotyping

Allele	Sequence (5'→ 3')	Amplicon Size
Chd4	TCC AGA AGA AGA CGG CAG AT	Wild-type: 275bp *Chd4* floxed allele: 400bp
	CTG GTC ATA GGG CAG GTC TC	
Ai9 tdTomato	AAG GGA GCT GCA GTG GAG TA	Wildtype: 287bp
	CCG AAA ATC TGT GGG AAG TC	
	GGC ATT AAA GCA GCG TAT CC	Ai9 allele: 196bp
	CTG TTC CTG TAC GGC ATG G	
Generic Cre	AGC GAT CGC TGC CAG GAT	Cre: 382bp
	ACC AGC GTT TTC GTT CTG CC	
Neurogenin1-specific Cre	AGC CCA TTC ACT CCC TGA G	Cre: 527bp
	ATC AAC GTT TTC TTT TCG GA	

Table 2. List of antibodies used for immunostaining and CUT&Tag

Antibody	Company	Identifier	Dilution	Purpose
mouse anti-CHD4	Abcam	Cat# ab70469, RRID: AB_2229454	1:100 (tissue) 1:300 (cells)	Immunostaining
rabbit anti-MYO7A	Proteus Bioscience	Cat# 25-6790, RRID: AB_10015251	1:200	Immunostaining
mouse anti-Tuj1 (TUBB3)	BioLegend	Cat# 801202, RRID: AB_10063408	1:300	Immunostaining
rabbit anti-Tuj1 (TUBB3)	BioLegend	Cat# 802001, RRID: AB_2564645	1:300	Immunostaining
rabbit anti-Sox2	Millipore	Cat# AB5603, RRID: AB_2286686	1:100	Immunostaining
Rabbit anti-RFP	Rockland	Cat# #600-401-379, RRID: AB_2209751	1:300	Immunostaining
goat anti-mouse Alexa 488	Thermo Fisher Scientific	Cat# A-11001, RRID: AB_2534069	1:500	Immunostaining
goat anti-mouse Alexa 647	Thermo Fisher Scientific	Cat# A-21235, RRID: AB_2535804	1:500	Immunostaining
goat anti-rabbit Alexa 488	Thermo Fisher Scientific	Cat# A-11034, RRID: AB_2576217	1:500	Immunostaining
goat anti-rabbit Alexa 647	Thermo Fisher Scientific	Cat# A-21246, RRID: AB_2535814	1:500	Immunostaining
goat anti-rabbit Alexa 568	Thermo Fisher Scientific	Cat# A-11011, RRID: AB_143157	1:500	Immunostaining
rabbit anti-p300	Santa Cruz Biotechnology	Cat # sc-585, RRID: AB_2231120	1:50	CUT&Tag
rabbit anti-H3K4me3	Active Motif	Cat# 39060, RRID: AB_2615077	1:50	CUT&Tag
rabbit anti-CHD4	Abcam	Cat# ab72418, RRID: AB_1268107	1:50	CUT&Tag
rabbit IgG	Jackson ImmunoResearch	Cat# 011-000-003, RRID: AB_2337118	1:50	CUT&Tag

Table 3. List of RNAscope probes used for smFISH

RNAscope Probe	Accession Number	Probe Region	Catalog Number	Company
Mm-Calb2-C2	NM_007586.1	147-1265	313641-C2	Advanced Cell Diagnostics, Inc.
Mm-Epha4	NM_007936.3	291-1191	419081	
Mm-Calb2-C3	NM_007586.1	147-1265	313641-C3	
Mm-Epha7-C2	NM_010141.4	1024-1981	430961-C2	
Mm-Efnb2	NM_010111.5	174-1316	477671	

959 **References**

960 Adamson, C. L., M. A. Reid, Z. L. Mo, J. Bowne-English and R. L. Davis (2002). "Firing features and
961 potassium channel content of murine spiral ganglion neurons vary with cochlear location." J Comp
962 Neurol **447**(4): 331-350.

963 Appler, J. M. and L. V. Goodrich (2011). "Connecting the ear to the brain: Molecular mechanisms of
964 auditory circuit assembly." Prog Neurobiol **93**(4): 488-508.

965 Bailey, T. L., J. Johnson, C. E. Grant and W. S. Noble (2015). "The MEME Suite." Nucleic Acids Res
966 **43**(W1): W39-49.

967 Borg, E., B. Engstrom, G. Linde and K. Marklund (1988). "Eighth nerve fiber firing features in normal-
968 hearing rabbits." Hear Res **36**(2-3): 191-201.

969 Bornelov, S., N. Reynolds, M. Xenophontos, S. Gharbi, E. Johnstone, R. Floyd, M. Ralser, J. Signolet,
970 R. Loos, S. Dietmann, P. Bertone and B. Hendrich (2018). "The Nucleosome Remodeling and
971 Deacetylation Complex Modulates Chromatin Structure at Sites of Active Transcription to Fine-Tune
972 Gene Expression." Mol Cell **71**(1): 56-72 e54.

973 Bruce, L. L., J. Kingsley, D. H. Nichols and B. Fritzsch (1997). "The development of vestibulocochlear
974 efferents and cochlear afferents in mice." Int J Dev Neurosci **15**(4-5): 671-692.

975 Chen, W. C., H. Z. Xue, Y. L. Hsu, Q. Liu, S. Patel and R. L. Davis (2011). "Complex distribution
976 patterns of voltage-gated calcium channel alpha-subunits in the spiral ganglion." Hear Res **278**(1-2):
977 52-68.

978 Clapier, C. R., J. Iwasa, B. R. Cairns and C. L. Peterson (2017). "Mechanisms of action and regulation
979 of ATP-dependent chromatin-remodelling complexes." Nat Rev Mol Cell Biol **18**(7): 407-422.

980 Coate, T. M. and M. W. Kelley (2013). "Making connections in the inner ear: recent insights into the
981 development of spiral ganglion neurons and their connectivity with sensory hair cells." Semin Cell Dev
982 Biol **24**(5): 460-469.

983 Coate, T. M., S. Raft, X. Zhao, A. K. Ryan, E. B. Crenshaw, 3rd and M. W. Kelley (2012). "Otic
984 mesenchyme cells regulate spiral ganglion axon fasciculation through a Pou3f4/EphA4 signaling
985 pathway." Neuron **73**(1): 49-63.

986 Coate, T. M., N. A. Spita, K. D. Zhang, K. T. Isgrig and M. W. Kelley (2015). "Neuropilin-2/Semaphorin-
987 3F-mediated repulsion promotes inner hair cell innervation by spiral ganglion neurons." Elife **4**.

988 Dabdoub, A., B. Fritzsch, A. N. Popper and R. R. Fay (2016). The primary auditory neurons of the
989 mammalian cochlea. New York, Springer.

990 Deans, M. R. (2022). "Planar cell polarity signaling guides cochlear innervation." Dev Biol **486**: 1-4.

991 Defourny, J., A. L. Poirrier, F. Lallemend, S. Mateo Sanchez, J. Neef, P. Vanderhaeghen, E. Soriano,
992 C. Peuckert, K. Kullander, B. Fritzsch, L. Nguyen, G. Moonen, T. Moser and B. Malgrange (2013).
993 "Ephrin-A5/EphA4 signalling controls specific afferent targeting to cochlear hair cells." Nat Commun **4**:
994 1438.

995 el Barbary, A. (1991). "Auditory nerve of the normal and jaundiced rat. I. Spontaneous discharge rate
996 and cochlear nerve histology." Hear Res **54**(1): 75-90.

997 Ghimire, S. R. and M. R. Deans (2019). "Frizzled3 and Frizzled6 Cooperate with Vangl2 to Direct
998 Cochlear Innervation by Type II Spiral Ganglion Neurons." J Neurosci **39**(41): 8013-8023.

999 Ghimire, S. R., E. M. Ratzan and M. R. Deans (2018). "A non-autonomous function of the core PCP
1000 protein VANGL2 directs peripheral axon turning in the developing cochlea." Development **145**(12).

1001 Gillespie, L. N., P. L. Marzella, G. M. Clark and J. M. Crook (2005). "Netrin-1 as a guidance molecule in
1002 the postnatal rat cochlea." Hear Res **199**(1-2): 117-123.

1003 Hoffmeister, H., A. Fuchs, F. Erdel, S. Pinz, R. Grobner-Ferreira, A. Bruckmann, R. Deutzmann, U.
1004 Schwartz, R. Maldonado, C. Huber, A. S. Dendorfer, K. Rippe and G. Langst (2017). "CHD3 and CHD4
1005 form distinct NuRD complexes with different yet overlapping functionality." Nucleic Acids Res **45**(18):
1006 10534-10554.

1007 Hosokawa, H., T. Tanaka, Y. Suzuki, C. Iwamura, S. Ohkubo, K. Endoh, M. Kato, Y. Endo, A. Onodera,
1008 D. J. Tumes, A. Kanai, S. Sugano and T. Nakayama (2013). "Functionally distinct Gata3/Chd4
1009 complexes coordinately establish T helper 2 (Th2) cell identity." Proc Natl Acad Sci U S A **110**(12):
1010 4691-4696.

1011 Huang, D., B. T. Sherman and R. A. Lempicki (2009). "Systematic and integrative analysis of large
1012 gene lists using DAVID bioinformatics resources." Nat Protoc **4**(1): 44-57.

1013 Huang, L. C., M. Barclay, K. Lee, S. Peter, G. D. Housley, P. R. Thorne and J. M. Montgomery (2012).
1014 "Synaptic profiles during neurite extension, refinement and retraction in the developing cochlea." Neural
1015 Dev **7**: 38.

1016 Hung, H., R. Kohnken and J. Svaren (2012). "The nucleosome remodeling and deacetylase chromatin
1017 remodeling (NuRD) complex is required for peripheral nerve myelination." J Neurosci **32**(5): 1517-1527.

1018 Kaaij, L. J. T., F. Mohn, R. H. van der Weide, E. de Wit and M. Buhler (2019). "The ChAHP Complex
1019 Counteracts Chromatin Looping at CTCF Sites that Emerged from SINE Expansions in Mouse." Cell
1020 **178**(6): 1437-1451 e1414.

1021 Kania, A. and R. Klein (2016). "Mechanisms of ephrin-Eph signalling in development, physiology and
1022 disease." Nat Rev Mol Cell Biol **17**(4): 240-256.

1023 Kent, W. J., A. S. Zweig, G. Barber, A. S. Hinrichs and D. Karolchik (2010). "BigWig and BigBed:
1024 enabling browsing of large distributed datasets." Bioinformatics **26**(17): 2204-2207.

1025 Kiang, N. Y., R. R. Pfeiffer, W. B. Warr and A. S. Backus (1965). "Stimulus Coding in the Cochlear
1026 Nucleus." Ann Otol Rhinol Laryngol **74**: 463-485.

1027 Kim, E. J., K. Hori, A. Wyckoff, L. K. Dickel, E. J. Koundakjian, L. V. Goodrich and J. E. Johnson
1028 (2011). "Spatiotemporal fate map of neurogenin1 (Neurog1) lineages in the mouse central nervous
1029 system." J Comp Neurol **519**(7): 1355-1370.

1030 Kim, Y. J., L. A. Ibrahim, S. Z. Wang, W. Yuan, O. V. Evgrafov, J. A. Knowles, K. Wang, H. W. Tao and
1031 L. I. Zhang (2016). "EphA7 regulates spiral ganglion innervation of cochlear hair cells." Dev Neurobiol
1032 **76**(4): 452-469.

1033 Koundakjian, E. J., J. L. Appler and L. V. Goodrich (2007). "Auditory neurons make stereotyped wiring
1034 decisions before maturation of their targets." J Neurosci **27**(51): 14078-14088.

1035 Kwan, K. Y., J. Shen and D. P. Corey (2015). "C-MYC transcriptionally amplifies SOX2 target genes to
1036 regulate self-renewal in multipotent otic progenitor cells." Stem Cell Reports **4**(1): 47-60.

1037 Langmead, B. and S. L. Salzberg (2012). "Fast gapped-read alignment with Bowtie 2." Nat Methods
1038 **9**(4): 357-359.

1039 Laureano, A., J. Kim, E. Martinez and K. Y. Kwan (2023). "Chromodomain helicase DNA binding
1040 protein 4 in cell fate decisions." Hear Res **436**: 108813.

1041 Layman, W. S., M. A. Sauceda and J. Zuo (2013). "Epigenetic alterations by NuRD and PRC2 in the
1042 neonatal mouse cochlea." Hear Res **304**: 167-178.

1043 Layman, W. S. and J. Zuo (2014). "Epigenetic regulation in the inner ear and its potential roles in
1044 development, protection, and regeneration." Front Cell Neurosci **8**: 446.

1045 Li, H., B. Handsaker, A. Wysoker, T. Fennell, J. Ruan, N. Homer, G. Marth, G. Abecasis, R. Durbin and
1046 S. Genome Project Data Processing (2009). "The Sequence Alignment/Map format and SAMtools."
1047 Bioinformatics **25**(16): 2078-2079.

1048 Liberman, L. D., H. Wang and M. C. Liberman (2011). "Opposing gradients of ribbon size and AMPA
1049 receptor expression underlie sensitivity differences among cochlear-nerve/hair-cell synapses." J
1050 Neurosci **31**(3): 801-808.

1051 Liberman, M. C. (1978). "Auditory-nerve response from cats raised in a low-noise chamber." J Acoust
1052 Soc Am **63**(2): 442-455.

1053 Liberman, M. C. (1982). "Single-neuron labeling in the cat auditory nerve." Science **216**(4551): 1239-
1054 1241.

1055 Liu, Q., P. B. Manis and R. L. Davis (2014). "I h and HCN channels in murine spiral ganglion neurons:
1056 tonotopic variation, local heterogeneity, and kinetic model." J Assoc Res Otolaryngol **15**(4): 585-599.

1057 Liu, W. and R. L. Davis (2014). "Calretinin and calbindin distribution patterns specify subpopulations of
1058 type I and type II spiral ganglion neurons in postnatal murine cochlea." J Comp Neurol **522**(10): 2299-
1059 2318.

1060 Low, J. K., S. R. Webb, A. P. Silva, H. Saathoff, D. P. Ryan, M. Torrado, M. Brofelth, B. L. Parker, N. E.
1061 Shepherd and J. P. Mackay (2016). "CHD4 Is a Peripheral Component of the Nucleosome Remodeling
1062 and Deacetylase Complex." J Biol Chem **291**(30): 15853-15866.

1063 Lu, C. C., J. M. Appler, E. A. Houseman and L. V. Goodrich (2011). "Developmental profiling of spiral
1064 ganglion neurons reveals insights into auditory circuit assembly." J Neurosci **31**(30): 10903-10918.

1065 Madisen, L., T. A. Zwingman, S. M. Sunkin, S. W. Oh, H. A. Zariwala, H. Gu, L. L. Ng, R. D. Palmiter,
1066 M. J. Hawrylycz, A. R. Jones, E. S. Lein and H. Zeng (2010). "A robust and high-throughput Cre
1067 reporting and characterization system for the whole mouse brain." Nat Neurosci **13**(1): 133-140.

1068 Marques, J. G., B. E. Gryder, B. Pavlovic, Y. Chung, Q. A. Ngo, F. Frommelt, M. Gstaiger, Y. Song, K.
1069 Benischke, D. Laubscher, M. Wachtel, J. Khan and B. W. Schafer (2020). "NuRD subunit CHD4
1070 regulates super-enhancer accessibility in rhabdomyosarcoma and represents a general tumor
1071 dependency." Elife **9**.

1072 Martinez-Monedero, R., C. Liu, C. Weisz, P. Vyas, P. A. Fuchs and E. Glowatzki (2016). "GluA2-
1073 Containing AMPA Receptors Distinguish Ribbon-Associated from Ribbonless Afferent Contacts on Rat
1074 Cochlear Hair Cells." eNeuro **3**(2).

1075 Meers, M. P., T. D. Bryson, J. G. Henikoff and S. Henikoff (2019). "Improved CUT&RUN chromatin
1076 profiling tools." Elife **8**.

1077 Meers, M. P., D. Tenenbaum and S. Henikoff (2019). "Peak calling by Sparse Enrichment Analysis for
1078 CUT&RUN chromatin profiling." Epigenetics Chromatin **12**(1): 42.

1079 Micucci, J. A., E. D. Sperry and D. M. Martin (2015). "Chromodomain helicase DNA-binding proteins in
1080 stem cells and human developmental diseases." Stem Cells Dev **24**(8): 917-926.

1081 Millard, C. J., N. Varma, A. Saleh, K. Morris, P. J. Watson, A. R. Bottrill, L. Fairall, C. J. Smith and J. W.
1082 Schwabe (2016). "The structure of the core NuRD repression complex provides insights into its
1083 interaction with chromatin." Elife **5**: e13941.

1084 Morra, R., B. M. Lee, H. Shaw, R. Tuma and E. J. Mancini (2012). "Concerted action of the PHD,
1085 chromo and motor domains regulates the human chromatin remodelling ATPase CHD4." FEBS Lett
1086 **586**(16): 2513-2521.

1087 Moser, T., N. Karagulyan, J. Neef and L. M. Jaime Tobon (2023). "Diversity matters - extending sound
1088 intensity coding by inner hair cells via heterogeneous synapses." EMBO J **42**(23): e114587.

1089 Nitarska, J., J. G. Smith, W. T. Sherlock, M. M. Hillege, A. Nott, W. D. Barshop, A. A. Vashisht, J. A.
1090 Wohlschlegel, R. Mitter and A. Riccio (2016). "A Functional Switch of NuRD Chromatin Remodeling
1091 Complex Subunits Regulates Mouse Cortical Development." Cell Rep **17**(6): 1683-1698.

1092 Nystrom, S. L. and D. J. McKay (2021). "Memes: A motif analysis environment in R using tools from the
1093 MEME Suite." PLoS Comput Biol **17**(9): e1008991.

1094 Pan, M. R., H. J. Hsieh, H. Dai, W. C. Hung, K. Li, G. Peng and S. Y. Lin (2012). "Chromodomain
1095 helicase DNA-binding protein 4 (CHD4) regulates homologous recombination DNA repair, and its
1096 deficiency sensitizes cells to poly(ADP-ribose) polymerase (PARP) inhibitor treatment." J Biol Chem
1097 **287**(9): 6764-6772.

1098 Petitpre, C., H. Wu, A. Sharma, A. Tokarska, P. Fontanet, Y. Wang, F. Helmbacher, K. Yackle, G.
1099 Silberberg, S. Hadjab and F. Lallemend (2018). "Neuronal heterogeneity and stereotyped connectivity
1100 in the auditory afferent system." Nat Commun **9**(1): 3691.

1101 Polo, S. E., A. Kaidi, L. Baskcomb, Y. Galanty and S. P. Jackson (2010). "Regulation of DNA-damage
1102 responses and cell-cycle progression by the chromatin remodelling factor CHD4." EMBO J **29**(18):
1103 3130-3139.

1104 Quinlan, A. R. and I. M. Hall (2010). "BEDTools: a flexible suite of utilities for comparing genomic
1105 features." Bioinformatics **26**(6): 841-842.

1106 Raft, S., E. J. Koundakjian, H. Quinones, C. S. Jayasena, L. V. Goodrich, J. E. Johnson, N. Segil and
1107 A. K. Groves (2007). "Cross-regulation of Ngn1 and Math1 coordinates the production of neurons and
1108 sensory hair cells during inner ear development." Development **134**(24): 4405-4415.

1109 Raj, A. and A. van Oudenaarden (2008). "Nature, nurture, or chance: stochastic gene expression and
1110 its consequences." Cell **135**(2): 216-226.

1111 Ramirez, F., F. Dundar, S. Diehl, B. A. Gruning and T. Manke (2014). "deepTools: a flexible platform for
1112 exploring deep-sequencing data." Nucleic Acids Res **42**(Web Server issue): W187-191.

1113 Reid, X. J., Y. Zhong and J. P. Mackay (2024). "How does CHD4 slide nucleosomes?" Biochem Soc
1114 Trans **52**(5): 1995-2008.

1115 Robinson, J. T., H. Thorvaldsdottir, W. Winckler, M. Guttman, E. S. Lander, G. Getz and J. P. Mesirov
1116 (2011). "Integrative genomics viewer." Nat Biotechnol **29**(1): 24-26.

1117 Ruggero, M. A., P. A. Santi and N. C. Rich (1982). "Type II cochlear ganglion cells in the chinchilla."
1118 Hear Res **8**(3): 339-356.

1119 Salehi, P., M. X. Ge, U. Gundimeda, L. Michelle Baum, H. Lael Cantu, J. Lavinsky, L. Tao, A. Myint, C.
1120 Cruz, J. Wang, A. M. Nikolakopoulou, C. Abdala, M. W. Kelley, T. Ohyama, T. M. Coate and R. A.
1121 Friedman (2017). "Role of Neuropilin-1/Semaphorin-3A signaling in the functional and morphological
1122 integrity of the cochlea." PLoS Genet **13**(10): e1007048.

1123 Sanders, T. R. and M. W. Kelley (2022). "Specification of neuronal subtypes in the spiral ganglion
1124 begins prior to birth in the mouse." Proc Natl Acad Sci U S A **119**(48): e2203935119.

1125 Schmiedt, R. A. (1989). "Spontaneous rates, thresholds and tuning of auditory-nerve fibers in the gerbil:
1126 comparisons to cat data." Hear Res **42**(1): 23-35.

1127 Shrestha, B. R., C. Chia, L. Wu, S. G. Kujawa, M. C. Liberman and L. V. Goodrich (2018). "Sensory
1128 Neuron Diversity in the Inner Ear Is Shaped by Activity." Cell **174**(5): 1229-1246 e1217.

1129 Sifrim, A., M. P. Hitz, A. Wilsdon, J. Breckpot, S. H. Turki, B. Thienpont, J. McRae, T. W. Fitzgerald, T.
1130 Singh, G. J. Swaminathan, E. Prigmore, D. Rajan, H. Abdul-Khaliq, S. Banka, U. M. Bauer, J. Bentham,
1131 F. Berger, S. Bhattacharya, F. Bu'Lock, N. Canham, I. G. Colgiu, C. Cosgrove, H. Cox, I. Daehnert, A.
1132 Daly, J. Danesh, A. Fryer, M. Gewillig, E. Hobson, K. Hoff, T. Homfray, A. K. Kahlert, A. Ketley, H. H.
1133 Kramer, K. Lachlan, A. K. Lampe, J. J. Louw, A. K. Manickara, D. Manase, K. P. McCarthy, K. Metcalfe,
1134 C. Moore, R. Newbury-Ecob, S. O. Omer, W. H. Ouwehand, S. M. Park, M. J. Parker, T. Pickardt, M. O.
1135 Pollard, L. Robert, D. J. Roberts, J. Sambrook, K. Setchfield, B. Stiller, C. Thornborough, O. Toka, H.
1136 Watkins, D. Williams, M. Wright, S. Mital, P. E. Daubeney, B. Keavney, J. Goodship, R. M. Abu-
1137 Sulaiman, S. Klaassen, C. F. Wright, H. V. Firth, J. C. Barrett, K. Devriendt, D. R. FitzPatrick, J. D.
1138 Brook and M. E. Hurles (2016). "Distinct genetic architectures for syndromic and nonsyndromic
1139 congenital heart defects identified by exome sequencing." Nat Genet **48**(9): 1060-1065.

1140 Sifrim, A., M. P. Hitz, A. Wilsdon, J. Breckpot, S. H. Turki, B. Thienpont, J. McRae, T. W. Fitzgerald, T.
1141 Singh, G. J. Swaminathan, E. Prigmore, D. Rajan, H. Abdul-Khaliq, S. Banka, U. M. Bauer, J. Bentham,
1142 F. Berger, S. Bhattacharya, F. Bu'Lock, N. Canham, I. G. Colgiu, C. Cosgrove, H. Cox, I. Daehnert, A.
1143 Daly, J. Danesh, A. Fryer, M. Gewillig, E. Hobson, K. Hoff, T. Homfray, I. Study, A. K. Kahlert, A.
1144 Ketley, H. H. Kramer, K. Lachlan, A. K. Lampe, J. J. Louw, A. K. Manickara, D. Manase, K. P.
1145 McCarthy, K. Metcalfe, C. Moore, R. Newbury-Ecob, S. O. Omer, W. H. Ouwehand, S. M. Park, M. J.
1146 Parker, T. Pickardt, M. O. Pollard, L. Robert, D. J. Roberts, J. Sambrook, K. Setchfield, B. Stiller, C.
1147 Thornborough, O. Toka, H. Watkins, D. Williams, M. Wright, S. Mital, P. E. Daubeney, B. Keavney, J.
1148 Goodship, U. K. Consortium, R. M. Abu-Sulaiman, S. Klaassen, C. F. Wright, H. V. Firth, J. C. Barrett,
1149 K. Devriendt, D. R. FitzPatrick, J. D. Brook, S. Deciphering Developmental Disorders and M. E. Hurles
1150 (2016). "Distinct genetic architectures for syndromic and nonsyndromic congenital heart defects
1151 identified by exome sequencing." Nat Genet **48**(9): 1060-1065.

1152 Sitko, A. A. and L. V. Goodrich (2021). "Making sense of neural development by comparing wiring
1153 strategies for seeing and hearing." Science **371**(6525).

1154 Spoendlin, H. (1972). "Innervation densities of the cochlea." Acta Otolaryngol **73**(2): 235-248.

1155 Sun, Y., L. Wang, T. Zhu, B. Wu, G. Wang, Z. Luo, C. Li, W. Wei and Z. Liu (2022). "Single-cell
1156 transcriptomic landscapes of the otic neuronal lineage at multiple early embryonic ages." Cell Rep
1157 **38**(12): 110542.

1158 Taberner, A. M. and M. C. Liberman (2005). "Response properties of single auditory nerve fibers in the
1159 mouse." J Neurophysiol **93**(1): 557-569.

1160 Tong, J. K., C. A. Hassig, G. R. Schnitzler, R. E. Kingston and S. L. Schreiber (1998). "Chromatin
1161 deacetylation by an ATP-dependent nucleosome remodelling complex." Nature **395**(6705): 917-921.

1162 Torchy, M. P., A. Hamiche and B. P. Klaholz (2015). "Structure and function insights into the NuRD
1163 chromatin remodeling complex." Cell Mol Life Sci **72**(13): 2491-2507.

1164 Toriello, H. V., W. Reardon, R. J. Gorlin and R. J. Gorlin (2004). Hereditary hearing loss and its
1165 syndromes. Oxford ; New York, Oxford University Press.

1166 Torrado, M., J. K. K. Low, A. P. G. Silva, J. W. Schmidberger, M. Sana, M. Sharifi Tabar, M. E. Isilak,
1167 C. S. Winning, C. Kwong, M. J. Bedward, M. J. Sperlazza, D. C. Williams, Jr., N. E. Shepherd and J. P.
1168 Mackay (2017). "Refinement of the subunit interaction network within the nucleosome remodelling and
1169 deacetylase (NuRD) complex." FEBS J **284**(24): 4216-4232.

1170 Wang, X., C. Xie, K. Shen, D. Li and X. S. Xie (2025). "Quantification and potential functional relevance
1171 of binding cooperativity of adjacent transcription factors on DNA." Proc Natl Acad Sci U S A **122**(18):
1172 e2422555122.

1173 Watson, A. A., P. Mahajan, H. D. Mertens, M. J. Deery, W. Zhang, P. Pham, X. Du, T. Bartke, W.
1174 Zhang, C. Edlich, G. Berridge, Y. Chen, N. A. Burgess-Brown, T. Kouzarides, N. Wiechens, T. Owen-
1175 Hughes, D. I. Svergun, O. Gileadi and E. D. Laue (2012). "The PHD and chromo domains regulate the
1176 ATPase activity of the human chromatin remodeler CHD4." J Mol Biol **422**(1): 3-17.

1177 Weiss, K., H. P. Lazar, A. Kurolap, A. F. Martinez, T. Paperna, L. Cohen, M. F. Smeland, S. Whalen, S.
1178 Heide, B. Keren, P. Terhal, M. Irving, M. Takaku, J. D. Roberts, R. M. Petrovich, S. A. Schrier Vergano,
1179 A. Kenney, H. Hove, E. DeChene, S. C. Quinonez, E. Colin, A. Ziegler, M. Rumple, M. Jain, D. Monteil,

1180 E. R. Roeder, K. Nugent, A. van Haeringen, M. Gambello, A. Santani, L. Medne, B. Krock, C. M.
1181 Skraban, E. H. Zackai, H. A. Dubbs, T. Smol, J. Ghoumid, M. J. Parker, M. Wright, P. Turnpenny, J.
1182 Clayton-Smith, K. Metcalfe, H. Kurumizaka, B. D. Gelb, H. Baris Feldman, P. M. Campeau, M. Muenke,
1183 P. A. Wade and K. Lachlan (2020). "The CHD4-related syndrome: a comprehensive investigation of the
1184 clinical spectrum, genotype-phenotype correlations, and molecular basis." Genet Med **22**(2): 389-397.

1185 Weiss, K., P. A. Terhal, L. Cohen, M. Bruccoleri, M. Irving, A. F. Martinez, J. A. Rosenfeld, K. Machol,
1186 Y. Yang, P. Liu, M. Walkiewicz, J. Beuten, N. Gomez-Ospina, K. Haude, C. T. Fong, G. M. Enns, J. A.
1187 Bernstein, J. Fan, G. Gotway, M. Ghorbani, D. D. D. Study, K. van Gassen, G. R. Monroe, G. van
1188 Haaften, L. Basel-Vanagaite, X. J. Yang, P. M. Campeau and M. Muenke (2016). "De Novo Mutations
1189 in CHD4, an ATP-Dependent Chromatin Remodeler Gene, Cause an Intellectual Disability Syndrome
1190 with Distinctive Dysmorphisms." Am J Hum Genet **99**(4): 934-941.

1191 Weisz, C. J., M. Lehar, H. Hiel, E. Glowatzki and P. A. Fuchs (2012). "Synaptic transfer from outer hair
1192 cells to type II afferent fibers in the rat cochlea." J Neurosci **32**(28): 9528-9536.

1193 Williams, C. J., T. Naito, P. G. Arco, J. R. Seavitt, S. M. Cashman, B. De Souza, X. Qi, P. Keables, U.
1194 H. Von Andrian and K. Georgopoulos (2004). "The chromatin remodeler Mi-2beta is required for CD4
1195 expression and T cell development." Immunity **20**(6): 719-733.

1196 Winter, I. M., D. Robertson and G. K. Yates (1990). "Diversity of characteristic frequency rate-intensity
1197 functions in guinea pig auditory nerve fibres." Hear Res **45**(3): 191-202.

1198 Xia, L., W. Huang, M. Bellani, M. M. Seidman, K. Wu, D. Fan, Y. Nie, Y. Cai, Y. W. Zhang, L. R. Yu, H.
1199 Li, C. A. Zahnow, W. Xie, R. W. Chiu Yen, F. V. Rassool and S. B. Baylin (2017). "CHD4 Has
1200 Oncogenic Functions in Initiating and Maintaining Epigenetic Suppression of Multiple Tumor
1201 Suppressor Genes." Cancer Cell **31**(5): 653-668 e657.

1202 Xue, Y., J. Wong, G. T. Moreno, M. K. Young, J. Cote and W. Wang (1998). "NURD, a novel complex
1203 with both ATP-dependent chromatin-remodeling and histone deacetylase activities." Mol Cell **2**(6): 851-
1204 861.

1205 Yang, Y., T. Yamada, K. K. Hill, M. Hemberg, N. C. Reddy, H. Y. Cho, A. N. Guthrie, A. Oldenborg, S.
1206 A. Heiney, S. Ohmae, J. F. Medina, T. E. Holy and A. Bonni (2016). "Chromatin remodeling inactivates
1207 activity genes and regulates neural coding." Science **353**(6296): 300-305.

1208 Yoshida, T., Y. Hu, Z. Zhang, A. O. Emmanuel, K. Galani, B. Muhire, H. J. Snippert, C. J. Williams, M.
1209 Y. Tolstorukov, F. Gounari and K. Georgopoulos (2019). "Chromatin restriction by the nucleosome
1210 remodeler Mi-2beta and functional interplay with lineage-specific transcription regulators control B-cell
1211 differentiation." Genes Dev **33**(13-14): 763-781.

1212 Zhang, K. D. and T. M. Coate (2017). "Recent advances in the development and function of type II
1213 spiral ganglion neurons in the mammalian inner ear." Semin Cell Dev Biol **65**: 80-87.

1214 Zhang, Y., G. LeRoy, H. P. Seelig, W. S. Lane and D. Reinberg (1998). "The dermatomyositis-specific
1215 autoantigen Mi2 is a component of a complex containing histone deacetylase and nucleosome
1216 remodeling activities." Cell **95**(2): 279-289.

1217 Zhu, L. J., C. Gazin, N. D. Lawson, H. Pages, S. M. Lin, D. S. Lapointe and M. R. Green (2010).
1218 "ChIPpeakAnno: a Bioconductor package to annotate ChIP-seq and ChIP-chip data." BMC
1219 Bioinformatics **11**: 237.